energies

MDPI

Article

Cooling Optimization Strategy for a 6s4p Lithium-Ion Battery Pack Based on Triple-Step Nonlinear Method

Hongya Zhang, Hao Chen and Haisheng Fang *

School of Energy and Power Engineering, Huazhong University of Science & Technology, Wuhan 430074, China
* Correspondence: hafang@hust.edu.cn

Abstract: In a battery cooling system, by adopting a cooling optimization control strategy, the battery temperature under different external environments and load currents can be adjusted to ensure performance and safety. In this study, two modes of the thermal management system are established for the 6s4p (six serial and four parallel batteries in a stage) battery pack. A single particle model, considering battery aging, is adopted for the battery. Furthermore, a cooling optimization control strategy for the battery is proposed based on the triple-step nonlinear method, and then the optimization effect is validated under two C-rate charge–discharge cycles, NEDC cycles, and US06 cycles. Moreover, an extended PID control strategy is constructed and compared with the triple-step nonlinear method. A comparison of pump power, thermal behavior, and aging performance indicate parallel cooling is more advantageous. This verifies the validity of the triple-step nonlinear method and shows its advantages over the extended PID method. The present study provides a method to investigate the thermal behavior and aging performance of a battery pack in a BTM system, and fills in the research gaps in the cooling optimization control strategy for battery packs.

Keywords: Li-ion battery; battery thermal management; triple-step nonlinear method; extended PID method; cooling optimization

Citation: Zhang, H.; Chen, H.; Fang, H. Cooling Optimization Strategy for a 6s4p Lithium-Ion Battery Pack Based on Triple-Step Nonlinear Method. *Energies* **2023**, *16*, 460. https://doi.org/10.3390/en16010460

Academic Editors: Linjing Zhang, Ning Li and Zhaoxia Peng

Received: 30 November 2022
Revised: 22 December 2022
Accepted: 28 December 2022
Published: 31 December 2022

1. Introduction

The vigorous development and widespread introduction of electric vehicles (EVs) have placed higher requirements on the driving endurance and safety performance of EVs [1]. Lithium-ion batteries (LIBs) are widely used in the automobile industry and in energy storage due to their high energy density [2,3]. However, the size and number of batteries cannot be increased indefinitely due to the limitations in vehicle space. Therefore, increasing the energy density and power density of batteries has become a priority to improve the driving endurance of EVs [4]. As the energy density and power density of the battery increase, the heat generation also increases. This requires an effective cooling method to dissipate the large amount of heat accumulated inside the battery over time [5]. Otherwise, the battery temperature will rise sharply and the battery capacity will continuously decline. In severe cases, it may even lead to thermal runaway or fire and explosion [6,7]. In addition, there are also many studies on the generation of LIBs for systematic research [8,9].

Many investigations have been conducted to better understand and improve battery performance. Some researchers have established battery thermal management (BTM) systems to control the temperature [10–13]. Studies of BTM system include air-cooling [14,15], liquid-cooling [16,17], phase-change material cooling [18,19], heat pipe-cooling [20,21], and cooling systems combined with the aforementioned methods [22–24]. Other researchers have studied the internal aging mechanism and battery aging to lay a foundation for the design of BTM systems [25,26]. Birkl et al. [27] summarized the causes, mechanisms, modes, and effects of battery aging. The causes trigger the mechanisms, and the mechanisms contribute to the modes of aging. The aging modes can be divided into three categories: loss of lithium inventory, loss of active material of the negative electrode (NE), loss of

active material of the and positive electrode (PE). These modes contribute to the aging of the battery and the battery capacities decline. A widely studied aging mechanism is the formation of a solid electrolyte interface (SEI) [28,29]. The charge–discharge rate (C-rate, defined as the measurement of the charge and discharge speed, which equals the current required for the battery to charge or discharge its capacity in a specified time) and ambient temperature are generally considered to be the important factors affecting the aging mechanisms [30,31]. Many experimental studies on battery aging and thermal management systems have been conducted. However, experiments on thermal management systems are complicated and time-consuming, especially when multiple charge–discharge cycle tests are required to consider battery aging. Numerical simulations of BTM systems under different EV-related cycle conditions are efficient and low-cost as they can reduce the number of experiments [32].

The difficulty in the simulation of LIBs is related to their multi-domain and multi-physics characteristics. Therefore, various battery models have been used to characterize the performance of LIBs, and these models have been developed to study electrochemical performance [33], aging [34], and even thermal runaway [35]. The single particle (SP) model is a commonly-used reduced-order electrochemical model, which was proposed by Haran et al. [36] based on the pseudo-two-dimensional model of Doyle–Fuller–Newman [37]. In the SP model, it is assumed that both electrodes are composed of multiple spherical particles of uniform size and the current is uniformly distributed on both electrodes. Therefore, each electrode can be approximated as a single spherical particle. The SP model is described by a set of ordinary differential equations, and it is derived directly from a comprehensive electrochemical model, thus explicitly preserving many important battery properties with high computational efficiency. The disadvantage of the SP model is that the electrolyte physics and degradation are not considered, so the accuracy at high C-rates is affected. Many researchers have established advanced SP models to address this deficiency.

Rahimian et al. [38] compared the SP model with a semi-empirical equivalent circuit model to predict battery voltages under constant current charge and discharge for different LIB datasets. The results showed that the SP model outperforms the equivalent circuit model in its predictive power for all datasets, while the computation time of both models was on the same order of magnitude. Li et al. [39] developed an aging model based on the SP model considering SEI layer formation and the stress due to the volume expansion of the particles in the active material. The Li-ion loss model due to SEI layer formation was integrated with an advanced SP model that incorporates electrolytic physics. This model can rapidly predict capacity fade and voltage profile changes as a function of cycle number and temperature with high accuracy. Richardson et al. [40] compared the SP model and the Doyle–Fuller–Newman model for different electrode materials, including lithium nickel manganese cobalt oxide, graphite, and lithium iron phosphate (LFP). Motivated by these differences, correction terms for the SP model were derived. Incorporating this into the SP model resulted in a corrected SP model that was significantly more accurate than the original SP model. Ren et al. [41] proposed an extended SP model with higher accuracy. Based on this model, a new state of charge (SOC) closed-loop estimation algorithm model was constructed. The results showed that the extended SP model can effectively simulate the performance of the battery, and the closed-loop SOC estimation algorithm can correct the initial SOC error without increasing the computational complexity.

In the modeling of the BTM system, in addition to the selection and optimization of a battery model to ensure the accuracy of the simulation, it is also necessary to select an appropriate cooling method. As mentioned above, the current main cooling methods for batteries are air cooling and liquid cooling. However, the research on battery cooling mainly focuses on the structural design and analysis of factors, and research on the optimization and control strategy of battery cooling is still in its infancy. Ji et al. [42] proposed an active temperature control method to equalize the temperature distribution of the batteries by adjusting the coolant flow rate. The optimal cooling flow rate was determined by setting different coolant flow rates to find the lowest battery temperature. This method is

complex and costly and is not suitable for complicated operating conditions. Zhu et al. [43] presented a finite-set-based model predictive control strategy for the BTM in hybrid EVs and verified the strategy under different cycle conditions. However, due to a large amount of computational data and high hardware requirements, this optimization process using dynamic programming algorithms was complicated. Ma et al. [44] proposed a cooling optimization strategy for LIBs based on the triple-step nonlinear method and compared the strategy with the PID method under NEDC and US06 cycle conditions. The results showed that the proposed method ensures a stable operating temperature and cooling process of LIBs. Ma et al. [45] further proposed a nonlinear model predictive control to optimize the cooling process of the battery module. The simulation results showed that the nonlinear model predictive control method ensured that the battery works near a target temperature under different working conditions. However, the battery model used in these studies was a lumped thermal model, which cannot reflect the electrochemical performance and aging of the battery. Moreover, the proposed cooling optimization strategies have only been used for the verification of a single battery, and the effect of applying a battery pack has not been studied.

As mentioned above, the advanced SP model is rarely used in the modeling of a BTM system and the cooling optimization strategy has been verified only for a single battery, which limits the application in real scenarios. Therefore, the gaps and deficiencies that are present in the literature are investigated in this study. First, a one-dimensional thermal management model of the 6s4p (six serial and four parallel batteries in a stage) battery pack is established for the first time based on our previous work [32]. The SP model, with a consideration of battery aging, is adopted to the 6s4p battery pack, so the electrochemical performance and degradation of each cell can be obtained more accurately. Secondly, two modes of the thermal management system are developed for the 6s4p battery pack, namely, a series cooling circuit and a parallel cooling circuit. The thermal behavior and aging performance of the battery pack under these two cooling modes are analyzed and compared. Thirdly, a cooling optimization control strategy for the key battery in the 6s4p battery pack is first proposed based on the triple-step nonlinear method, and then the optimization effect of this strategy in the battery pack is validated under two C-rate charge–discharge cycles, NEDC cycles, and US06 cycles. Finally, an extended PID control strategy is constructed and compared with the triple-step nonlinear method to verify the effects of and differences between the two strategies. The present study provides a method to investigate the thermal behavior and aging performance of the battery pack in a BTM system, and fills in the research gaps in cooling optimization for battery packs. The results in the present study demonstrate application of system modeling and the optimization of an automotive battery pack, and are applicable to the design of BTM systems.

2. Materials and Methods

2.1. Charge–Discharge and Nominal Electrochemical Model of the Battery Cell

The characteristics and the geometry of the LFP battery have been discussed in our previous work [29] and are listed in Table 1. The electrochemical reactions can be expressed as in [46].

The reaction at the positive electrode is:

$$\mathrm{Li}_{1-i}\mathrm{FePO}_4 + i\mathrm{Li}^+ + i\mathrm{e}^- \underset{\text{charge}}{\overset{\text{discharge}}{\rightleftharpoons}} \mathrm{LiFePO}_4 \quad (1)$$

The reaction at the negative electrode is:

$$\mathrm{Li}_j\mathrm{C}_6 \underset{\text{charge}}{\overset{\text{discharge}}{\rightleftharpoons}} \mathrm{Li}_{1-j}\mathrm{C}_6 + j\mathrm{Li}^+ + j\mathrm{e}^- \quad (2)$$

Table 1. The technical specifications and thermophysical parameters of the battery cell.

Parameter	Value
Cell length	140 mm
Cell width	70 mm
Cell thickness	7 mm
Nominal voltage	3.2 V
Charge cut-off voltage	3.65 V
Discharge cut-off voltage	2 V
Nominal capacity	5 A·h
Energy density	245 $Wh \cdot L^{-1}$
Positive electrode material	$LiFePO_4$
Negative electrode material	Graphite-based carbon
Electrolyte material	Carbonate based
Thermal conductivity, k_b ($W \cdot m^{-1} \cdot K^{-1}$)	55.66
Density, ρ_b ($kg \cdot m^{-3}$)	2318.07
Specific thermal capacity, $C_{p,b}$ ($J \cdot kg^{-1} \cdot K^{-1}$)	1056.08

Figure 1a shows the charge–discharge model of the battery, including the battery model, thermal boundary condition, electrical connection, and cycle signal of the charge–discharge process. The thermophysical parameters are described by the material parameters module (listed in Table 1) and the part of the battery in contact with the air is described by the ambient conditions module, as shown in Figure 1a. The equation can be expressed as:

$$Q_{tra} = h_{conv} A_b (T_b - T_{amb}) + \sigma_B \chi \left(T_b^4 - T_{amb}^4 \right) \quad (3)$$

where Q_{tra} is the heat transferred from the battery to the ambient air. h_{conv} is the convective heat transfer coefficient and χ is the surface emissivity, and they are set as 10 $W \cdot m^{-2} \cdot K^{-1}$ [32] and 0.8 [47], respectively. A_b is the area between the battery and the ambient air. σ_B is the Stefan–Boltzmann constant. T_b and T_{amb} are the battery temperature and ambient temperature, respectively. The electrochemical model chosen is a simplification of the pseudo-two-dimensional model (proposed by Doyle–Fuller–Newman [37] and described in detail in our previous work [48]) called the single particle (SP) model where the solid phase is modeled as a single particle, as shown in Figure 1b. This model has been widely used in the one-dimensional simulation software, AMESim (Advanced Modeling Environment for performing Simulation of engineering systems). The thickness direction contains five parts: a negative current collector (NCC), a negative electrode (NE), a separator (SEP), a positive electrode (PE), and a positive current collector (PCC), as shown in Figure 1b. In the SP model, the electrode is regarded as the superposition of two continuums, namely the electrolytic phase and a solid matrix, as shown in Figure 1b. The models of solid matrices are microscopic spherical particles in which Li-ions diffuse and react on the surface of the spheres. The main hypotheses [49] of this model are:

(1) The passive sign convention is used: $I > 0$ during charge and $I < 0$ during discharge;
(2) The particles in both electrodes can be represented as two mean spherical particles;
(3) The active surface is assumed to be same in all areas: $S_p = S_{sep} = S_n = A_{ele}$.

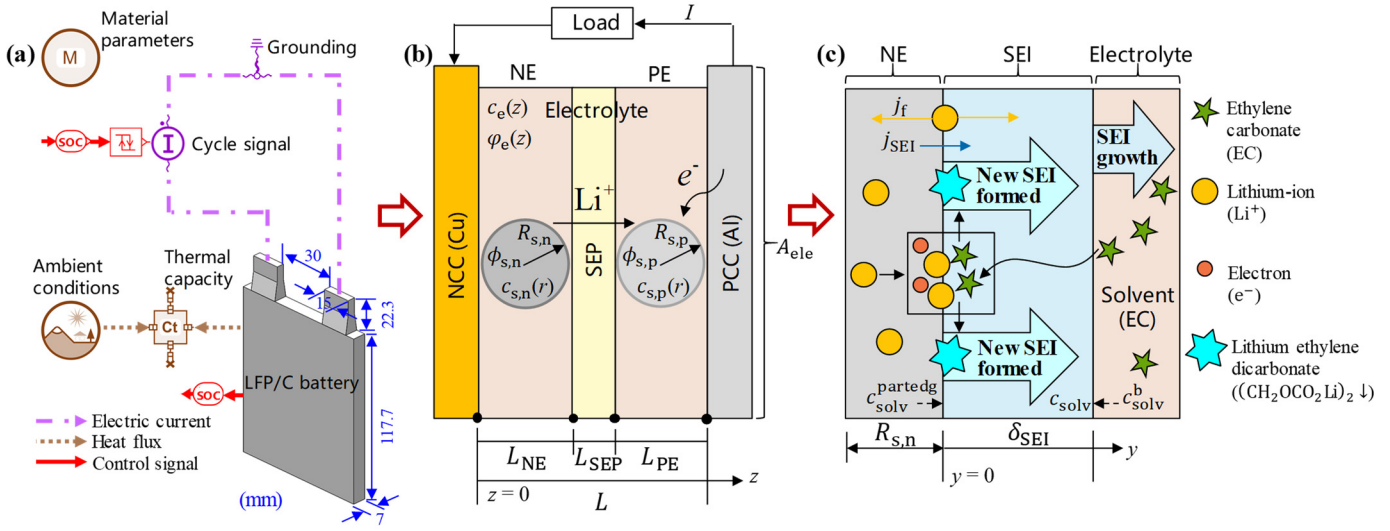

Figure 1. Model diagram of the battery: (**a**) charge and discharge model; (**b**) electrochemical model (SP model); and (**c**) aging model (SEI layer formation on the negative electrode).

The SP model computes the battery voltage based on its internal state and external solicitations. The voltage is the difference between the potential of its electrodes summed with the electrolyte potential [50]:

$$U(t) = \phi_s(L) - \phi_s(0) = U_p - U_n + \eta(L) - \eta(0) + \phi_e(L) - \phi_e(0), \quad (4)$$

where U_p and U_n are the thermodynamic potential of the PE and NE, respectively. $\eta(L)$ and $\eta(0)$ are the overpotentials at $z = L$ and $z = 0$, respectively. z is the battery thickness direction, as shown in Figure 1b. $\phi_e(L)$ and $\phi_e(0)$ are the electrolyte potentials at $z = L$ and $z = 0$, respectively. Thermodynamic potentials are evaluated from the solid concentration of Li in the bulk ($R = 0$) of the single particle:

$$U_p = U_p^{ref}(x_p) = U_p^{ref}\left(\frac{c_{s,p}^b}{c_{s,p}^{max}}\right), \; U_n = U_n^{ref}(x_n) = U_n^{ref}\left(\frac{c_{s,n}^b}{c_{s,n}^{max}}\right), \quad (5)$$

where $\frac{c_{s,p}^b}{c_{s,p}^{max}}$ and $\frac{c_{s,n}^b}{c_{s,n}^{max}}$ correspond to the coefficients i and j used in Equations (1) and (2), respectively. $c_{s,p}^b$ and $c_{s,n}^b$ are the bulk Li concentrations in the solid phase for PE and NE, respectively. $c_{s,p}^{max}$ and $c_{s,n}^{max}$ are the maximum Li concentrations in the PE and NE, respectively. U_p^{ref} and U_n^{ref} are the reference potentials of the PE and NE, respectively. The nominal physical and chemical phenomena occurring in Li-ion systems can be expressed by the mass conservation of Li^+ species, charge conservation, and electrochemical kinetics, as shown in Table 2. All these equations are coupled into the framework of the P2D electrochemical model and have been discussed in previous works [45,48].

Table 2. Equations in the electrochemical model.

Physical and Chemical Mechanisms	Equations	Boundary Conditions
Solid phase: conservation of Li^+ species	$\frac{\partial}{\partial t}c_s - \frac{1}{r^2}\frac{\partial}{\partial r}\left(r^2 D_s \frac{\partial}{\partial r}c_s\right) = 0$	$D_s \frac{\partial}{\partial r}c_s\Big\|_{r=0} = 0, \; -D_s \frac{\partial}{\partial r}c_s\Big\|_{r=R_s} = \frac{j_f}{a_s F}$
Electrolyte phase: conservation of Li^+ species	$\frac{\partial}{\partial t}\varepsilon_e c_e - \frac{\partial}{\partial z}\left(D_e^{eff}\frac{\partial}{\partial z}c_e\right) - (1 - t_+)\frac{j_f}{F} = 0$	$\frac{\partial}{\partial z}c_e\Big\|_{z=0} = \frac{\partial}{\partial z}c_e\Big\|_{z=L} = 0$

Table 2. *Cont.*

Physical and Chemical Mechanisms	Equations	Boundary Conditions
Solid phase: charge conservation	$\frac{\partial}{\partial z}\left(\sigma^{\text{eff}}\frac{\partial}{\partial z}\phi_{\text{s}}\right)-j_{\text{f}}=0$	$-\sigma_{\text{e}}^{\text{eff}}\frac{\partial}{\partial z}\phi_{\text{s}}\Big\|_{z=0}=-\sigma^{\text{eff}}\frac{\partial}{\partial z}\phi_{\text{s}}\Big\|_{z=L}=\frac{I}{A_{\text{ele}}}$, $\frac{\partial}{\partial z}\phi_{\text{s}}\Big\|_{z=L_{\text{NE}}}=\frac{\partial}{\partial z}\phi_{\text{s}}\Big\|_{z=L-L_{\text{PE}}}=0$
Electrolyte phase: charge conservation	$\frac{\partial}{\partial z}\left(\kappa^{\text{eff}}\frac{\partial}{\partial z}\phi_{\text{e}}\right)+\frac{\partial}{\partial z}\left(\kappa_{D}^{\text{eff}}\frac{\partial}{\partial z}\ln c_{\text{e}}\right)+j_{\text{f}}=0$	$\frac{\partial}{\partial z}\phi_{\text{e}}\Big\|_{z=0}=\frac{\partial}{\partial z}\phi_{\text{e}}\Big\|_{z=L}=0$
Electrochemical kinetics	$j_{\text{f}}=a_{\text{s}}i_{0}\left[\exp\left(\frac{\alpha_{\text{ox}}F}{RT}\eta\right)-\exp\left(\frac{-\alpha_{\text{red}}F}{RT}\eta\right)\right]$	
Electrolyte ionic diffusivity	$D_{\text{e}}^{\text{eff}}$=$D_{\text{e}}\varepsilon_{\text{e}}^{\gamma_{\text{e}}}$	
Electrolyte ionic conductivity	$\kappa^{\text{eff}}=\kappa\varepsilon_{\text{e}}^{\gamma_{\text{e}}}$	
Electrolyte ionic diffusional conductivity	$\kappa_{D}^{\text{eff}}=\frac{2RT}{F}\kappa^{\text{eff}}(t_{+}-1)\left(1+\frac{d\ln f_{\pm}}{d\ln c_{\text{e}}}\right)$	
Solid phase electronic conductivity	$\sigma^{\text{eff}}=\sigma{\varepsilon_{\text{s}}}^{\gamma_{\text{s}}}$	
Specific interfacial surface area	$a_{\text{s}}=\frac{3\varepsilon_{\text{s}}}{R_{\text{s}}}$	

The diffusion of the solid phase leads to solid phase overpotential, which can be approximated as the difference between the bulk thermodynamic potential and the thermodynamic potential at the surface of the particles [50]:

$$U_{\text{p}}=U_{\text{p}}^{\text{ref}}(x_{\text{p}})=U_{\text{p}}^{\text{ref}}\left(\frac{c_{\text{s,p}}^{\text{b}}}{c_{\text{s,p}}^{\text{max}}}\right),\ U_{\text{n}}=U_{\text{n}}^{\text{ref}}(x_{\text{n}})=U_{\text{n}}^{\text{ref}}\left(\frac{c_{\text{s,n}}^{\text{b}}}{c_{\text{s,n}}^{\text{max}}}\right),\tag{6}$$

where $c_{\text{s,p}}^{R_{\text{s,p}}}$ and $c_{\text{s,n}}^{R_{\text{s,n}}}$ are the Li concentrations at the solid–electrolyte interface phase, where the subscripts p and n denote PE and NE, respectively. The solid ohmic overpotentials can be calculated as [50]:

$$U_{\text{p}}=U_{\text{p}}^{\text{ref}}(x_{\text{p}})=U_{\text{p}}^{\text{ref}}\left(\frac{c_{\text{s,p}}^{\text{b}}}{c_{\text{s,p}}^{\text{max}}}\right),\ U_{\text{n}}=U_{\text{n}}^{\text{ref}}(x_{\text{n}})=U_{\text{n}}^{\text{ref}}\left(\frac{c_{\text{s,n}}^{\text{b}}}{c_{\text{s,n}}^{\text{max}}}\right),\tag{7}$$

where $\sigma_{\text{p}}^{\text{eff}}$ and $\sigma_{\text{n}}^{\text{eff}}$ are the effective solid phase conductivities of the PE and NE, respectively. L_{PE} and L_{NE} are the thicknesses of the PE and NE, respectively. I is the electric current and A_{ele} is the geometric area of the electrodes. The electrolyte diffusion overpotential due to the Li concentration gradient in the electrolyte can be calculated as [50]:

$$\eta_{\text{e}}^{\text{diff}}=(1-t_{+})2\frac{RT}{F}\ln\frac{c_{\text{e}}(L)}{c_{\text{e}}(0)},\tag{8}$$

where t_{+} is the Li transference number. $c_{\text{e}}(L)$ and $c_{\text{e}}(0)$ are the Li concentrations in the electrolyte phase at $z = L$ and $z = 0$, respectively. R is the ideal gas constant, T is the temperature, and F is the Faraday constant. The electrolyte ohmic overpotential due to electrolyte conductivity can be calculated as [50]:

$$\eta_{\text{e}}^{\text{ohm}}=\frac{I}{2A_{\text{ele}}}\left(\frac{L_{\text{NE}}}{\kappa_{\text{n}}^{\text{eff}}}+\frac{2L_{\text{SEP}}}{\kappa_{\text{SEP}}^{\text{eff}}}+\frac{L_{\text{PE}}}{\kappa_{\text{p}}^{\text{eff}}}\right),\tag{9}$$

where $\kappa_{\text{n}}^{\text{eff}}$, $\kappa_{\text{SEP}}^{\text{eff}}$, and $\kappa_{\text{p}}^{\text{eff}}$ are the electrolyte effective ionic conductivities in the NE, SEP, and PE, respectively. L_{SEP} is the thickness of SEP. The oxidation and reduction charge transfer coefficients, α_{ox} and α_{red}, are assumed to be equal to 0.5 for both electrodes. The positive and negative kinetic overpotentials can be expressed as [50]:

$$\eta_{\text{p}}^{\text{k}}=2\frac{RT}{F}\ln\left(\xi_{\text{p}}+\sqrt{\xi_{\text{p}}^{2}+1}\right),\eta_{\text{n}}^{\text{k}}=2\frac{RT}{F}\ln\left(\xi_{\text{n}}+\sqrt{\xi_{\text{n}}^{2}+1}\right),\tag{10}$$

where

$$\xi_{\mathrm{p}} = \frac{I}{2i_{0,\mathrm{p}}S_{\mathrm{p}}} = \frac{R_{\mathrm{s,p}}}{6\varepsilon_{\mathrm{s,p}}i_{0,\mathrm{p}}A_{\mathrm{ele}}L_{\mathrm{PE}}}I,\ \xi_{\mathrm{n}} = \frac{I}{2i_{0,\mathrm{p}}S_{\mathrm{n}}} = \frac{R_{\mathrm{s,n}}}{6\varepsilon_{\mathrm{s,n}}i_{0,\mathrm{n}}A_{\mathrm{ele}}L_{\mathrm{NE}}}I, \tag{11}$$

where S_{p} and S_{n} are the area of PE and NE, respectively. $R_{\mathrm{s,p}}$ and $R_{\mathrm{s,n}}$ are the particle radii in the PE and NE, respectively. $\varepsilon_{\mathrm{s,p}}$ and $\varepsilon_{\mathrm{s,n}}$ are the volume fractions of the active material in the PE and NE, respectively. The exchange current densities can be expressed as [50]:

$$\begin{aligned} i_{0,\mathrm{p}} &= k_{0,\mathrm{p}}F(c_{\mathrm{e}})^{\alpha_{\mathrm{ox,p}}}\left(c_{\mathrm{s,p}}^{R_{\mathrm{s,p}}}\right)^{\alpha_{\mathrm{ox,p}}}\left(c_{\mathrm{s,p}}^{\max} - c_{\mathrm{s,p}}^{R_{\mathrm{s,p}}}\right)^{\alpha_{\mathrm{ox,p}}} \\ i_{0,\mathrm{n}} &= k_{0,\mathrm{n}}F(c_{\mathrm{e}})^{\alpha_{\mathrm{ox,n}}}\left(c_{\mathrm{s,n}}^{R_{\mathrm{s,n}}}\right)^{\alpha_{\mathrm{ox,n}}}\left(c_{\mathrm{s,n}}^{\max} - c_{\mathrm{s,n}}^{R_{\mathrm{s,n}}}\right)^{\alpha_{\mathrm{ox,n}}}, \end{aligned} \tag{12}$$

where c_{e} is the Li-ion concentration in the electrolyte phase and $\alpha_{\mathrm{ox,p}}$ and $\alpha_{\mathrm{ox,n}}$ represent the oxidation charge transfer coefficients of the PE and NE, respectively. $k_{0,\mathrm{p}}$ and $k_{0,\mathrm{n}}$ are the reaction rate constants of the PE and NE, respectively. By combining these equations, the output voltage (Equation (4)) of the battery can be expressed as:

$$U(t) = U_{\mathrm{p}}^{\mathrm{ref}}\left(\frac{c_{\mathrm{s,p}}^{R_{\mathrm{s,p}}}}{c_{\mathrm{s,p}}^{\max}}\right) - U_{\mathrm{n}}^{\mathrm{ref}}\left(\frac{c_{\mathrm{s,n}}^{R_{\mathrm{s,n}}}}{c_{\mathrm{s,n}}^{\max}}\right) + \eta_{\mathrm{s,p}}^{\mathrm{ohm}} - \eta_{\mathrm{s,n}}^{\mathrm{ohm}} + \eta_{\mathrm{e}}^{\mathrm{ohm}} + \eta_{\mathrm{e}}^{\mathrm{diff}} + \eta_{\mathrm{p}}^{\mathrm{k}} - \eta_{\mathrm{n}}^{\mathrm{k}} \tag{13}$$

It is important to note that Equation (13) does not take into account the battery aging. The expression of battery voltage considering the battery aging is shown in Equation (20).

2.2. Aging Model of the Battery Cell

Battery aging results in capacity and power losses due to several physical mechanisms. The physical mechanism taken into account in this study is the formation of a solid electrolyte interface (SEI) layer on the NE. In addition, its effects on the battery behavior are considered. SEI layer formation is a phenomenon occurring on a negative carbonaceous electrode when its potential is low [49]. Under these conditions, Li starts a reaction with the solvent of the electrolyte which forms the SEI, as shown in Figure 1c. The reaction equation is [51]:

$$2\mathrm{EC} + 2\mathrm{e}^{-} + 2\mathrm{Li}^{+} \Rightarrow (\mathrm{CH_2OCO_2Li})_2 \downarrow + \mathrm{C_2H_4} \uparrow \tag{14}$$

During this reaction, lithium is withdrawn from the NE and trapped in the SEI. This leads to a loss of cycling Li and thus a capacity loss. In addition, the SEI formed is a resistive layer leading to an increase in the resistance. As described in Figure 1c, the electrolyte solvent is transported from the electrolyte bulk to the particle surface of the SEI, it then reacts and forms a new SEI. Equations involved in the aging calculation have been comprehensively discussed in previous work [48] and are listed here in Table 3.

Table 3. Equations solved for the aging model.

Physical and Chemical Mechanisms	Equations	Boundary Conditions
SEI formation reaction kinetics	$j_{\mathrm{SEI}} = 2Fk_{\mathrm{SEI}}c_{\mathrm{solv}}^{\mathrm{partedg}}c_{\mathrm{s,n}}(r=R_{\mathrm{s,n}})^2 \exp\left(-\frac{\beta_{\mathrm{SEI}}F}{RT}\cdot\left(\frac{-\delta_{\mathrm{SEI}}I}{\kappa_{\mathrm{SEI}}S_{\mathrm{n}}}\right)\right) \exp\left(-\frac{\beta_{\mathrm{SEI}}F}{RT}(\phi_{\mathrm{s,n}} - U_{\mathrm{SEI}})\right)$	
Solvent diffusion in the SEI	$\frac{\partial c_{\mathrm{solv}}}{\partial t} = D_{\mathrm{solv}}\frac{\partial^2 c_{\mathrm{solv}}}{\partial y^2} - \frac{d\delta_{\mathrm{SEI}}}{dt}\frac{\partial c_{\mathrm{solv}}}{\partial y}$	$D_{\mathrm{solv}}\frac{\partial c_{\mathrm{solv}}}{\partial y}\Big\vert_{y=R_{\mathrm{s,n}}} - \frac{d\delta_{\mathrm{SEI}}}{dt}c_{\mathrm{solv}}^{\mathrm{partedg}} = -\frac{j_{\mathrm{SEI}}}{2F}$, $c_{\mathrm{solv}}(r=R_{\mathrm{s,n}}+\delta_{\mathrm{SEI}}) = \varepsilon_{\mathrm{SEI}}c_{\mathrm{solv}}^{\mathrm{b}}$
Loss of capacity variation	$\frac{dC_{\mathrm{loss}}^{\mathrm{SEI}}}{dt} = \frac{j_{\mathrm{SEI}}S_{\mathrm{n}}}{3600}$ $\mathrm{LOC_{SEI}} = \frac{C_{\mathrm{loss}}^{\mathrm{SEI}}}{C_{\mathrm{tot}}} \times 100$	
SEI porosity variation	$\frac{d\varepsilon_{\mathrm{SEI}}}{dt} = \frac{-j_{\mathrm{SEI}}S_{\mathrm{n}}}{3600C_{\mathrm{loss}}^{\mathrm{SEI}}}(1-\varepsilon_{\mathrm{SEI}})\left(1-\frac{1-\varepsilon_{\mathrm{SEI}}}{1-\varepsilon_{\mathrm{SEI}}^{*}}\right)$	
SEI layer thickness	$\delta_{\mathrm{SEI}} = \frac{3600C_{\mathrm{loss}}^{\mathrm{SEI}}M_{\mathrm{SEI}}}{2F\rho_{\mathrm{SEI}}S_{\mathrm{n}}(1-\varepsilon_{\mathrm{SEI}})}$	

It is worth mentioning that $\varepsilon^{*}_{\mathrm{SEI}}$ is the instantaneously formed SEI layer porosity. $\varepsilon_{\mathrm{SEI}}$ is the SEI layer porosity. The ohmic overvoltage can be calculated as [52]:

$$\eta_{\mathrm{SEI}} = -\frac{\delta_{\mathrm{SEI}}}{\kappa_{\mathrm{SEI}} S_{\mathrm{n}}} I,\ \kappa_{\mathrm{SEI}} = \kappa_{\mathrm{SEI,data}} (1-\varepsilon_{\mathrm{SEI}})^{\gamma_{\mathrm{SEI}}}, \tag{15}$$

where $\kappa_{\mathrm{SEI,data}}$ is the index of the SEI layer electronic conductivity data and γ_{SEI} is the SEI Bruggeman exponent. c_{solv} is the concentration of the solvent inside the SEI layer. The bulk solvent concentration, $c^{\mathrm{b}}_{\mathrm{solv}}$, is considered to be constant outside the SEI layer, as shown in Figure 1c. Based on these equations, it is possible to evaluate the solvent concentration, c_{solv}, and then the parasitic current of the SEI formation, j_{SEI}, can be calculated. Furthermore, the variation in the SEI porosity, capacity loss, and the SEI layer thickness can be calculated.

For dynamic aging modeling, when the model is initialized, previous aging needs to be taken into account. Firstly, based on the initial capacity loss, the initial insertion rate of the NE can be modified as:

$$x_{\mathrm{n,int}} = x_{\mathrm{n},0} + \frac{3600 \frac{\mathrm{SOC_{int}}}{100} \left(C_{\mathrm{nom}} - C^{\mathrm{SEI}}_{\mathrm{loss,int}} \right)}{A_{\mathrm{ele}} L_{\mathrm{NE}} \varepsilon_{\mathrm{s,n}} F c^{\mathrm{max}}_{\mathrm{s,n}}}, \tag{16}$$

where $x_{\mathrm{n},0}$ is the negative insertion rate when the state of charge is zero (SOC = 0), $\mathrm{SOC_{int}}$ is the initial SOC, C_{nom} is the nominal capacity, and $C^{\mathrm{SEI}}_{\mathrm{loss,int}}$ is the initial cycling Li loss due to SEI formation. Secondly, using the bulk solvent concentration and the battery average temperature, the initial solvent concentrations in the SEI layers can be calculated. With the assumption of a stationary state, it is assumed that the input current is 0 A and all time derivatives are null.

$$\frac{d\varepsilon_{\mathrm{SEI}}}{dt} = 0,\ \frac{\partial c_{\mathrm{solv}}}{\partial t} = 0 \tag{17}$$

There are several different consequences of aging on cell behavior. First, the current resulting from the parasitic reaction needs to be taken into account in the solid phase Li conservation. Therefore, the boundary condition of solid-phase Li^{+} conservation in Table 2 can be modified as:

$$-D_{\mathrm{s}} \frac{\partial c_{\mathrm{s,n}}}{\partial r}\bigg|_{r=R_{\mathrm{s}}} = \frac{j_{\mathrm{f}}}{a_{\mathrm{s}} F} + \frac{j_{\mathrm{SEI}}}{F} \tag{18}$$

Then, the porosity of the NE is modified due to the clogging of pores by the SEI layer [52]:

$$\varepsilon_{\mathrm{e,n}} = \varepsilon_{\mathrm{e,n,int}} - \varepsilon_{\mathrm{s,n}} \frac{3\delta_{\mathrm{SEI}}(t)}{R_{\mathrm{s,n}}}, \tag{19}$$

where $\varepsilon_{\mathrm{e,n,int}}$ is the initial porosity of the NE. In the event of a SEI layer that is too thick, the porosity is completely clogged. At this point, the battery reaches the end of its life and the model stops. The final effect is the increase in resistance due to the growth of the SEI layer. Another ohmic drop is added to the final voltage to take into account the effect of the SEI on the cell voltage; therefore, Equation (13) can be modified as:

$$U(t) = U^{\mathrm{ref}}_{\mathrm{p}} \left(\frac{c^{R_{\mathrm{s,p}}}_{\mathrm{s,p}}}{c^{\mathrm{max}}_{\mathrm{s,p}}} \right) - U^{\mathrm{ref}}_{\mathrm{n}} \left(\frac{c^{R_{\mathrm{s,n}}}_{\mathrm{s,n}}}{c^{\mathrm{max}}_{\mathrm{s,n}}} \right) + \eta^{\mathrm{ohm}}_{\mathrm{s,p}} - \eta^{\mathrm{ohm}}_{\mathrm{s,n}} + \eta^{\mathrm{ohm}}_{\mathrm{e}} + \eta^{\mathrm{diff}}_{\mathrm{e}} + \eta^{\mathrm{k}}_{\mathrm{p}} - \eta^{\mathrm{k}}_{\mathrm{n}} - \eta_{\mathrm{SEI}} \tag{20}$$

The total current intensity in the NE can be expressed as:

$$j_{\mathrm{tot}} = j_{\mathrm{f}} + a_{\mathrm{s,n}} j_{\mathrm{SEI}} \tag{21}$$

2.3. Thermal Models of the Battery Cell

The generated heat is described classically as the sum of irreversible and reversible heats [52]:

$$Q_{\text{gen}} = -\left(\left(\eta_{\text{s,p}}^{\text{ohm}} - \eta_{\text{s,n}}^{\text{ohm}} + \eta_{\text{e}}^{\text{ohm}} + \eta_{\text{e}}^{\text{diff}} + \eta_{\text{p}}^{\text{k}} - \eta_{\text{n}}^{\text{k}} - \eta_{\text{SEI}}\right) I + T\left(\frac{dU_{\text{p}}}{dT}(x_{\text{p}}) - \frac{dU_{\text{n}}}{dT}(x_{\text{n}})\right) I\right), \tag{22}$$

the first and second items on the right are the Joule effect and entropic effect in the battery, respectively. The equation of convective and radiative heat transfer is shown in Equation (3). Therefore, the energy balance of the battery cell can be expressed as:

$$\frac{d}{dt}T = \frac{1}{m_{\text{b}} C_{\text{pb}}}(Q_{\text{gen}} - Q_{\text{tra}}), \tag{23}$$

where m_{b} and C_{pb} are the mass and specific thermal capacity of the battery cell, respectively. The nominal electrochemical model, thermal model, and aging model are coupled to study the battery performance. Several parameters are temperature dependent, and the Arrhenius law [52–54] can be used to evaluate these parameters, as shown in Table 4. The parameters of the battery model are summarized in Table 5.

Table 4. Equations for the temperature-dependent parameters.

Parameters	Equations	Refs.
	Active material in solid phase	
Solid phase diffusivity (D_{s})	$D_{\text{s,p}} = 5.9 \times 10^{-20} \exp\left(-\frac{50{,}000}{8.314}\left(\frac{1}{T} - \frac{1}{298}\right)\right)$	[50,52]
	$D_{\text{s,n}} = 3 \times 10^{-15} \exp\left(-\frac{35{,}000}{8.314}\left(\frac{1}{T} - \frac{1}{298}\right)\right)$	[50,52]
Solid phase conductivity (σ)	$\sigma_{\text{p}} = 0.7 \exp\left(-\frac{10{,}000}{8.314}\left(\frac{1}{T} - \frac{1}{298}\right)\right)$	[50,52]
	$\sigma_{\text{n}} = 100 \exp\left(-\frac{11{,}000}{8.314}\left(\frac{1}{T} - \frac{1}{298}\right)\right)$	[50,52]
Electrode reaction rate constant (k_0)		[50,52]
	$k_{0,\text{n}} = 1.5 \times 10^{-10} \exp\left(-\frac{20{,}000}{8.314}\left(\frac{1}{T} - \frac{1}{298}\right)\right)$	[50,52]
	Electrolyte	
Electrolyte ionic diffusivity (D_{e})	$D_{\text{e}} = 1 \times 10^{-4} \times 10^{-4.43 - \frac{54}{T-229}} \exp\left(-\frac{c_{\text{e}}}{-0.26795T^2 + 169.99T - 25{,}342}\right)$	[50,52]
Electrolyte ionic conductivity (κ)	$\kappa = (-1.5069 \times 10^{-2} + 8.8078 \times 10^{-5}T - 9.4814 \times 10^{-8}T^2)c_{\text{e}} \exp((-1.5799 \times 10^{-3} + 7.8183 \times 10^{-6}T - 1.0513 \times 10^{-8}T^2){c_{\text{e}}}^{1.2167})$	[50,52]
	SEI formation	
SEI formation reaction rate constant (k_{SEI})	$k_{\text{SEI}} = 2.9465 \times 10^{-26} \exp\left(-\frac{149{,}150}{8.314}\left(\frac{1}{T} - \frac{1}{298}\right)\right)$	[50,52]
SEI solvent diffusivity (D_{solv})	$D_{\text{solv}} = 5.5098 \times 10^{-20} \exp\left(-\frac{79{,}781}{8.314}\left(\frac{1}{T} - \frac{1}{298}\right)\right)$	[50,52]
SEI conductivity (κ_{SEI})	$\kappa_{\text{SEI}} = 1.7 \times 10^{-4} \exp\left(-\frac{10{,}578}{8.314}\left(\frac{1}{T} - \frac{1}{298}\right)\right)$	[50,52]

Table 5. Parameters of the battery model.

Parameters	Value	Ref.
SOC_{int} (%)	100	Estimated
A_{ele} (m^2)	0.395	[51]
C_{nom} (A·h)	5	[51]
α_{ox}	0.5	[51]
α_{red}	0.5	[51]
R ($J \cdot mol^{-1} \cdot K^{-1}$)	8.314	
F ($C \cdot mol^{-1}$)	96,487	
Positive electrode		
L_{PE} (µm)	70	[51]
x_p at SOC 0%	0.74	[51]
x_p at SOC 100%	0.035	[51]
$\varepsilon_{e,p}$	0.332	[51]
$\varepsilon_{s,p}$	0.42	[51]
$R_{s,p}$ (µm)	0.11	[51]
$\gamma_{s,p}$	2.1	[51]
$c_{s,p}^{max}$ ($mol \cdot m^{-3}$)	22,806	[51]
Negative electrode		
S_n (m^2)	0.395	[51]
L_{NE} (µm)	34	[51]
x_n at SOC 0%	0.0132	[51]
x_n at SOC 100%	0.811	[51]
$\varepsilon_{e,n}$	0.33	[51]
$\varepsilon_{s,n}$	0.555	[51]
$R_{s,n}$ (µm)	5	[51]
$\gamma_{s,n}$	2.3	[51]
$c_{s,n}^{max}$ ($mol \cdot m^{-3}$)	31,370	[51]
Aging due to SEI layer formation		
$C_{loss,int}^{SEI}$ (A·h)	0.01	[52]
$\varepsilon_{SEI,int}$	0.01	[52]
U_{SEI} (V)	0.04	[52]
ρ_{SEI} ($kg \cdot m^{-3}$)	1690	[52]
c_{solv}^{b} ($mol \cdot m^{-3}$)	4541	[52]
β_{SEI}	0.5	[52]
γ_{SEI}	1.5	[52]
M_{SEI} ($kg \cdot mol^{-1}$)	0.162	[52]
ε_{SEI}^{*}	$\begin{cases} \varepsilon_{SEI}^{*} = 0.03\frac{I}{S_n} + 0.01 \left(0 \le \frac{I}{S_n} \le 6\right) \\ \varepsilon_{SEI}^{*} = 0.1525\frac{I}{S_n} - 0.725 \ (6 < \frac{I}{S_n} \le 10) \\ \varepsilon_{SEI}^{*} = 0.8 \ (10 < \frac{I}{S_n} \le 20) \end{cases}$	[52]
Electrolyte		
c_e ($mol \cdot m^{-3}$)	1200	[51]
t_+	0.363	[51]
Separator		
L_{SEP} (µm)	25	[51]
$\varepsilon_{e,sep}$	0.54	[51]
γ_{sep}	1.5	[51]

2.4. Thermal Management Model of the 6s4p Battery Pack

The three-dimensional thermal management model of the 6s4p battery pack has been proposed in our previous work [32]. On this basis, two modes of the thermal management system are developed for the 6s4p battery pack using AMESim (Advanced Modeling Environment for performing Simulation of engineering systems) in this study, as shown in Figure 2. The cooling circuits are connected in series (Figure 2a) or in parallel (Figure 2b).

Both modes of the thermal management system consist of four cold plates, a centrifugal pump, several thermal-hydraulic pipes, an expansion tank, a radiator, a fan, and a temperature sensor. Different colors and types of lines represent different kinds of connections, including electrical current, heat flow, control signals, and coolant. Every four battery cells in parallel are tightly packed and cooled by cold plates. The convective and radiative heat transfer equations are similar to that in Equation (3). The coolant was selected as a 50% volume concentration of ethylene glycol aqueous solution for the cooling system. The centrifugal pump is used to provide velocity to the coolant. Several thermal-hydraulic pipes connect the entire cooling circuit, and the expansion tank is used to stabilize hydraulic pressure throughout the circuit for safety. The radiator and fan are used to cool the coolant flows from the cold plates, and the temperature sensor is used to monitor the temperature of the coolant before it flows back to the centrifugal pump. Parameters of the cold plate, coolant, and ambient air are shown in Table 6. On this basis, 20 cases (cases A to T) were determined according to the C-rate and coolant mass flow rate, as shown in Table 7.

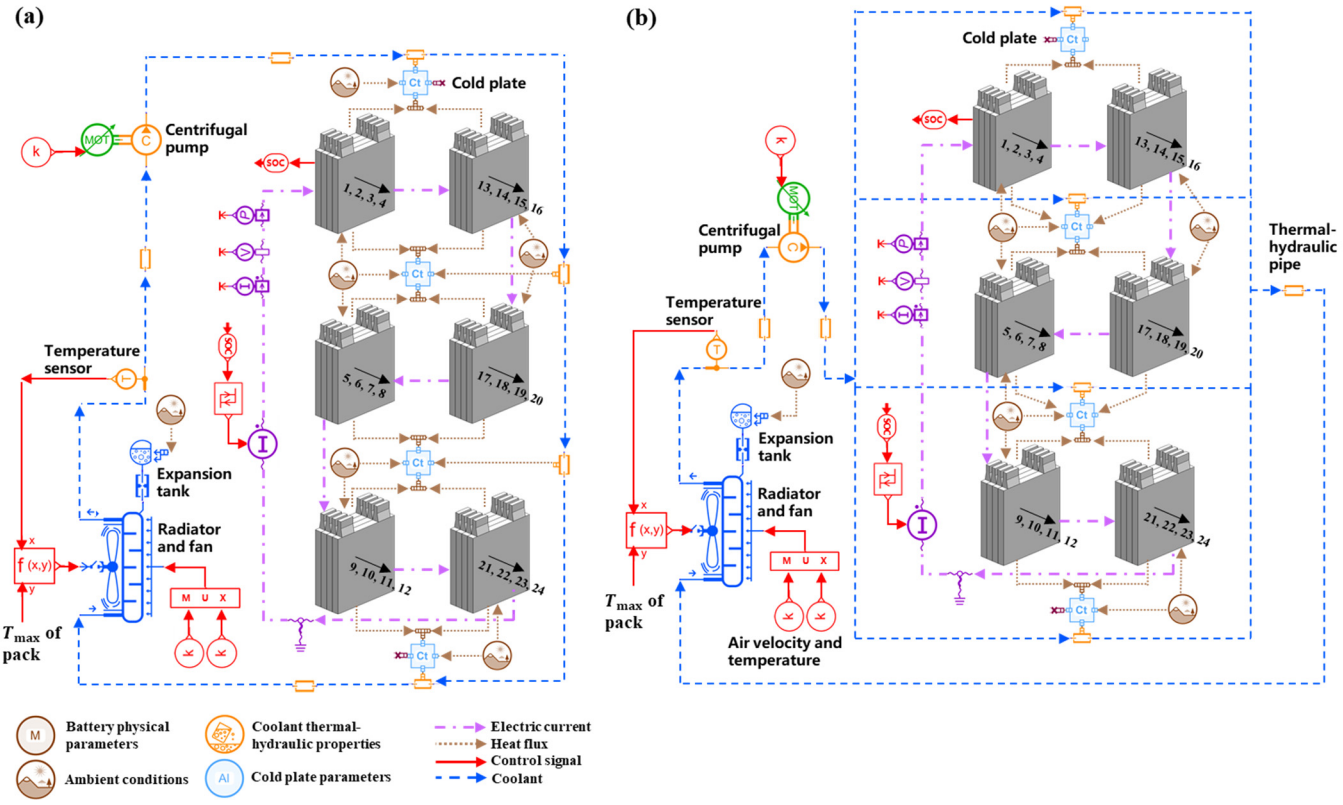

Figure 2. Two thermal management modes of the 6s4p battery pack: (**a**) series cooling circuit and (**b**) parallel cooling circuit.

Table 6. Thermal physical parameters for the cold plate, coolant, and ambient air.

Parameter	Cold Plate	Coolant	Ambient Air
Initial temperature (K)	298.15	298.15	298.15
Thermal conductivity, k ($W \cdot m^{-1} \cdot K^{-1}$)	237	0.4156	-
Density, ρ ($kg \cdot m^{-3}$)	2700	1069	1.1691
Specific thermal capacity, C_p ($J \cdot kg^{-1} \cdot K^{-1}$)	897	3310	-
Convective heat transfer coefficient, h ($W \cdot m^{-2} \cdot K^{-1}$)	-	-	10
Dynamic viscosity, μ_{co} ($kg \cdot m^{-1} \cdot s^{-1}$)	-	0.004563	

Table 7. Parameters for the two modes of thermal management system under different working conditions.

Cooling Type	Parallel		Series	
Pump rotary speed ($r \cdot min^{-1}$)	1000	3000	1000	3000
Mechanical power provided by the pump to the coolant (W)	7.168	218.873	2.620	81.552
Volumetric flow rate ($L \cdot min^{-1}$)	18.325 (4.581)	62.3352 (15.584)	6.65476	23.0198
Velocity ($m \cdot s^{-1}$)	3.868 (0.967)	13.153 (3.288)	1.404	4.858
Mass flow rate ($kg \cdot s^{-1}$) / C-rates	0.325 (0.081)	1.104 (0.276)	0.118	0.408
5 C	Case A	Case F	Case K	Case P
4 C	Case B	Case G	Case L	Case Q
3 C	Case C	Case H	Case M	Case R
2 C	Case D	Case I	Case N	Case S
1 C	Case E	Case J	Case O	Case T

2.5. Triple-Step Nonlinear Cooling Control Strategy

It can be observed from Figure 2b that the thermal management system of the 6s4p battery pack has a certain symmetry. The input parameters into the coupled model are the current and ambient temperature, and the output parameters are the voltage and temperature of the cell. The temperature of battery 6 is the highest due to its structural design. Therefore, batteries 5 and 6 were selected as the key batteries for the study of the cooling strategy. The thermal models of batteries 5 and 6 are shown in Figure 3a. It can be observed that the thermal models are extremely complicated due to the consideration of various thermal terms. However, the thermal model of a single battery is suitable for linearization under certain conditions, as shown in Figure 3b. Moreover, the heat generation of each cell is the same due to the use of the same coupled model and initial conditions, as shown in Figure 3c. Only the heat generation of the cell and the heat transfer with the coolant are considered; a similar simplification can be found in the literature [44].

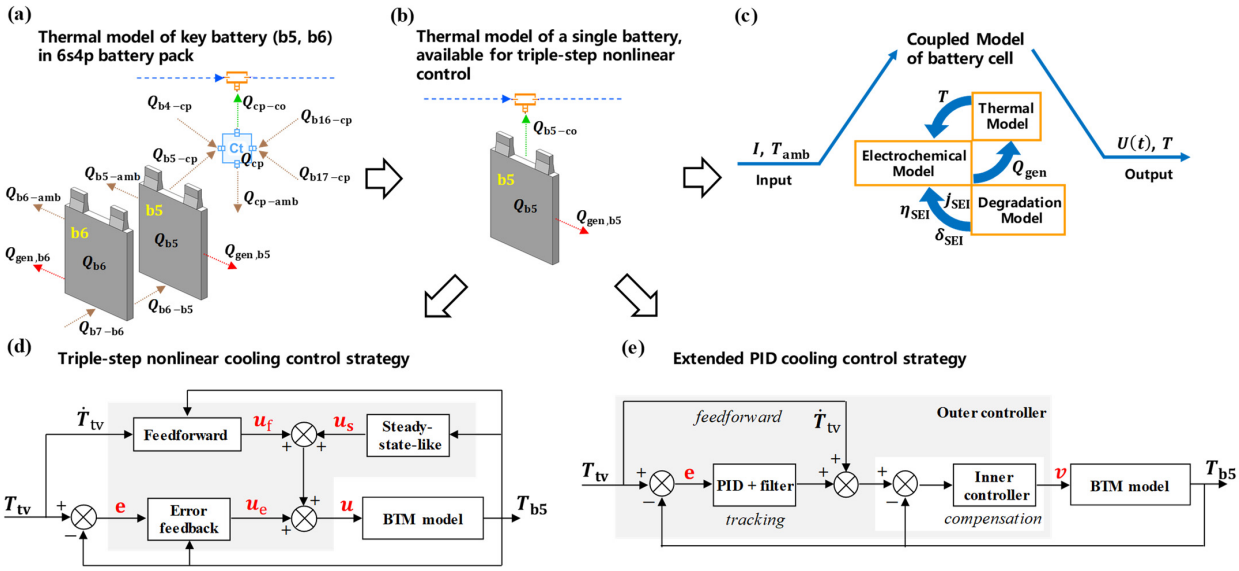

Figure 3. Battery thermal management model and control strategies: (**a**) schematic of battery thermal management model used in the study; (**b**) simplified battery thermal management model for designing a triple-step nonlinear control; (**c**) coupled model of the battery cell; (**d**) triple-step nonlinear cooling control strategy; and (**e**) extended PID cooling control strategy.

Based on the above model description and Figure 2b, battery 5 was selected for analysis of the cooling optimization strategy (see Figure 3b) and the thermal model can be expressed as:

$$Q_{b5} = m_b C_{p,b} \frac{d}{dt} T_{b5} = Q_{gen,\ b5} - Q_{b5-co}, \tag{24}$$

where Q_{b5}, $Q_{gen,\ b5}$, and Q_{b5-co} are the heat change, heat generation, and heat transferred from battery 5 to the coolant, respectively. According to the thermal model description and Equation (22), $Q_{gen,\ b5}$ can be simplified to:

$$Q_{gen,\ b5} = Q_{gen,\ b5} = U_{ir} I + U_r I T_{b5}, \tag{25}$$

where subscripts ir and r represent irreversible and reversible, respectively. Q_{b5-co} can be expressed as:

$$Q_{b5-co} = h_{b5-co} A_{b5-co} (T_{b5} - T_{co}), \tag{26}$$

where h_{b5-co} and A_{b5-co} are the heat transfer coefficient and the contact area between battery 5 and the coolant, respectively. T_{b5} and T_{co} are the temperature of battery 5 and the coolant, respectively. The heat transfer coefficient, h_{b5-co}, can be calculated as [55]:

$$h_{b5-co} = \frac{Nu_{co} \cdot k_{co}}{D}, \tag{27}$$

where Nu_{co} and k_{co} are the Nusselt number and the thermal conductivity of coolant, respectively. D is the equivalent diameter of the pipe, which is 35 mm. For the forced convection between the coolant and battery 5, turbulent flow is considered when the length of the pipe is much longer. Thus, Nu_{co} can be obtained by the experimental correlation of Sieder–Tate [56]:

$$Nu_{co} = 0.027 (Re_{co})^{0.8} (Pr_{co})^{\frac{1}{3}} \left(\frac{\mu_{co}}{\mu_w} \right)^{0.14}, \tag{28}$$

where Re_{co} and Pr_{co} are the Reynolds number and Prandtl number of the coolant, respectively. μ_{co} is the dynamic viscosity of the coolant and μ_w is the dynamic viscosity near the pipe wall. Re_{co} can be calculated as:

$$Re_{co} = \frac{\rho_{co} v_{co} D}{\mu_{co}}, \tag{29}$$

where ρ_{co} and v_{co} are the density and flow velocity of the coolant, respectively. From Equations (27)–(29), the heat transfer coefficient, h_{b5-co}, can be expressed as:

$$h_{b5-co} = \frac{0.027 (Re_{co})^{0.8} (Pr_{co})^{\frac{1}{3}} \left(\frac{\mu_{co}}{\mu_w} \right)^{0.14} k_{co}}{D} = a_1 {v_{co}}^{0.8}, \tag{30}$$

where $a_1 = \frac{0.027 (\rho_{co})^{0.8} (Pr_{co})^{\frac{1}{3}} k_{co}}{(\mu_{co})^{0.66} (\mu_w)^{0.14} D^{0.2}}$. Let $u = {v_{co}}^{0.8}$, from Equations (24)–(30), then the temperature of battery 5 (T_{b5}) can be expressed as:

$$\frac{d}{dt} T_{b5} = \frac{U_{ir} I + U_r I T_{b5}}{m_b C_{p,b}} - \frac{a_1 A_{b5-co} (T_{b5} - T_{co})}{m_b C_{p,b}} u \tag{31}$$

The input is the current load, I, and the coolant flow rate, v, and the output is the temperature of battery 5.

As mentioned above, a new cooling and control strategy should be proposed to avoid too much cooling or an excessive increase in battery temperature. Fortunately, a thermal model of a single battery is available for the design of triple-step nonlinear cooling control. After the triple-step nonlinear cooling control strategy was solved for battery 5, this strategy was applied to the 6s4p battery pack to validate its applicability. Moreover, an extended

PID cooling control strategy was also adopted to compare the results with those using a triple-step nonlinear cooling control strategy. Both the triple-step nonlinear method and extended PID method adjust the temperature of battery 5 by changing the coolant flow rate. The detailed design process is shown in Figure 4.

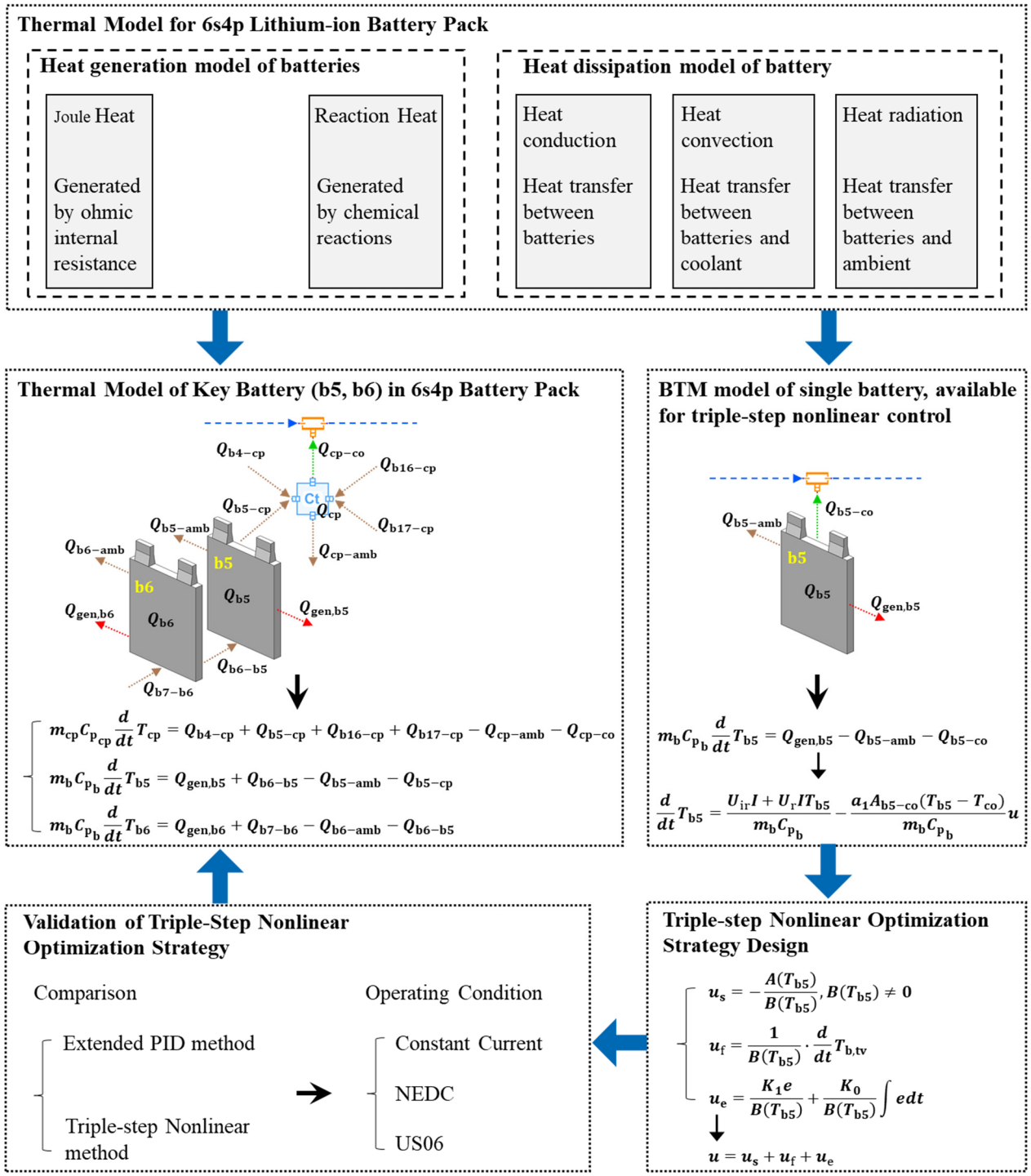

Figure 4. Optimization process for the key battery.

The design of steady state control, the reference variable feed-forward control, and the error feedback control are three main steps of the triple-step nonlinear method [44,57]. The design processes for battery 5 are illustrated in Figure 3d,e, respectively. T_{tv} is the target temperature of battery 5, T_{b5} is the actual temperature of battery 5, and u is a control

law. Let $A(T_{b5}) = \frac{U_{ir}I+U_rIT_{b5}}{m_bC_{p,b}}$, $B(T_{b5}) = -\frac{a_1A_{b5-co}(T_{b5}-T_{co})}{m_bC_{p,b}}$. Then, Equation (31) can be rewritten as:

$$\frac{d}{dt}T_{b5} = A(T_{b5}) + B(T_{b5})u \tag{32}$$

Equation (32) can be adapted to different methods [58].

Step 1: Steady-state-like Control.

The control law, u_s, changes dynamically with the output. The purpose of u_s is to gradually adjust the temperature of battery 5 to a stable state. When a stable state is reached, $\frac{d}{dt}T_{b5} = 0$, so combining Equations (31) and (32), we then obtain:

$$u_s = -\frac{A(T_{b5})}{B(T_{b5})} = \frac{U_{ir}I + U_rIT_{b5}}{a_1A_{b5-co}(T_{b5} - T_{co})}, B(T_{b5}) \neq 0 \tag{33}$$

Step 2: Reference Variable Feed-forward Control.

The target temperature, T_{tv}, is pre-set and has a prediction effect on its differential, $\frac{d}{dt}T_{tv}$. Therefore, introducing the tracking target temperature control law can effectively reduce the adjustment time. The control law, u_f, is added based on Step 1. By letting $\frac{d}{dt}T_{b5} = \frac{d}{dt}T_{tv}$, we obtain:

$$u = u_s + u_f \rightarrow u_f = \frac{1}{B(T_{b5})}\cdot\frac{d}{dt}T_{tv} = -\frac{m_bC_{p,b}}{a_1A_{b5-co}(T_{b5} - T_{co})}\cdot\frac{d}{dt}T_{tv} \tag{34}$$

Step 3: Error Feedback Control.

Based on the controller design method of the error system, the control law, u_e, is obtained. This control law can further reduce the impact caused by the external disturbance and modeling deviation of the system and guarantee the steady-state of the system.

$$u = u_s + u_f + u_e \rightarrow u_e = -\frac{1}{B(T_{b5})}\left(\frac{d}{dt}T_{tv} - \frac{d}{dt}T_{b5}\right) \tag{35}$$

The error is the deviation between the target temperature and actual temperature of battery 5:

$$e = T_{tv} - T_{b5} \tag{36}$$

Based on Equations (35) and (36), the derivative of the input deviation can be expressed as:

$$\frac{d}{dt}e = -B(T_{b5})u_e \tag{37}$$

The Lyapunov function is selected to solve the error feedback control law [44]:

$$V = \frac{1}{2}e^2 + \frac{1}{2}K_0\left(\int e dt\right)^2 \rightarrow \frac{d}{dt}V = e\cdot\frac{d}{dt}e + K_0e\int e dt \tag{38}$$

Let $\frac{d}{dt}V = -K_1e^2$, and combine Equations (37) and (38), then the control law can be expressed as:

$$-B(T_{b5})\cdot u_e = -K_1e - K_0\int e dt \tag{39}$$

where $K_1 > 0$ and $K_0 > 0$. When $\frac{d}{dt}V \leq 0$, a stable state is achieved. By simplifying Equation (39), the control law can be expressed as:

$$\begin{aligned} u_e = \frac{K_1e}{B(T_{b5})} + \frac{K_0}{B(T_{b5})}\int e dt \rightarrow u_e \\ = -\frac{m_bC_{p,b}K_1}{a_1A_{b5-co}(T_{b5}-T_{co})}e - \frac{m_bC_{p,b}K_0}{a_1A_{b5-co}(T_{b5}-T_{co})}\int e dt \end{aligned} \tag{40}$$

Equations (33), (34), and (40) are summarized as the final control law:

$$u = -\frac{A(T_{b5})}{B(T_{b5})} + \frac{1}{B(T_{b5})} \cdot \frac{d}{dt} T_{tv} + \frac{K_1 e}{B(T_{b5})} + \frac{K_0}{B(T_{b5})} \int e dt \tag{41}$$

The final control law is:

$$u = \frac{U_{ir} I + U_r I T_{b5}}{a_1 A_{b5-co}(T_{b5} - T_{co})} - \frac{m_b C_{p,b}}{a_1 A_{b5-co}(T_{b5} - T_{co})} \cdot \frac{d}{dt} T_{tv} - \frac{m_b C_{p,b} K_1}{a_1 A_{b5-co}(T_{b5} - T_{co})} e - \frac{m_b C_{p,b} K_0}{a_1 A_{b5-co}(T_{b5} - T_{co})} \int e dt \tag{42}$$

We now consider the system modeling error, di. Under the framework of state stability theory, the robust stability of the system needs to be analyzed. Let $\zeta = \int e dt$, then combining Equations (37) and (39), we obtain:

$$e = \dot{\zeta} \rightarrow \frac{de}{dt} = -K_1 e - K_0 \zeta + di, \tag{43}$$

and Equation (43) can be expressed in the matrix form as:

$$\frac{d\bar{e}}{dt} = H\bar{e} + Gdi, \tag{44}$$

where $\bar{e} = [\zeta \; e]^T$, $H = \begin{bmatrix} 0 & 1 \\ -K_0 & -K_1 \end{bmatrix}$, and $G = [0 \; 1]^T$. Equation (44) is a linear system. As mentioned above, in the description of the triple-step nonlinear method, the asymptotic stability of the system is demonstrated without considering the disturbance, di. According to the conclusion of input state stability of a linear system, the closed-loop system has robust stability [59].

3. Model Validation

The whole system is established in the one-dimensional software package AMESim, including the electrochemical model, thermal model, aging model, and cooling control model. Each module provided by AMESim is modeled based on physical mechanisms. The connection relationship between the modules in the system is stated in the above description, and the practicability of each module has been proven through extensive research [44,45,58]. Therefore, AMESim is an experimental platform that can be used to replace the real experimental platform to explore the battery performance in the thermal management system. Moreover, the model of a 5 A·h LFP/C battery at 25 °C was adopted for the validation of the battery model used in this study, as shown in Figure 5. The equipment used in the experiment has been introduced in previous work [51]. In this work, a cycle consists of a constant-current (CC) charging process and a constant-current discharging process. The experimental charge–discharge data were then compared with the simulated results in this study, as shown in Figure 6.

Figure 6a shows the voltage curves of the charge–discharge process at different C-rates. It can be seen that the simulated curves agree well with the experimental results. Then, the experimental temperature data at different C-rates were then compared with the simulated results, as shown in Figure 6b. The cell temperature can reach 47.5 °C at five C-rates after one cycle of the charge–discharge process. The temperature curves obtained by simulation at different C-rates were also in good agreement with the experimental values. Finally, the decrease in capacity was compared and validated. The aging mechanism of the SEI formation was considered in the simulations for all conditions. The initial capacity loss, $C_{loss,int}^{SEI}$, was 0.01 A·h according to the battery factory parameters, which was set as the initial condition in the modeling, as shown in Table 6. The loss of capacity (LOC) (the ratio of the lost capacity to nominal capacity, 5 A·h) was calculated by Equation (44) at different C-rates, and then compared with the experimental data, as shown in Figure 6c. The comparison presents good agreement, which indicates the model accuracy. The simulated

results were slightly different from the experimental data, which was possibly due to some model parameters not being totally applicable to the experimental tests. In addition, the initial conditions and boundary conditions of the battery in the experiment and simulation are not exactly the same. The simulated battery temperature was also compared with that in the literature [32,60] during the charge–discharge process, showing a good agreement. For example, the battery temperature in Figure 6b is verified in the literature [32].

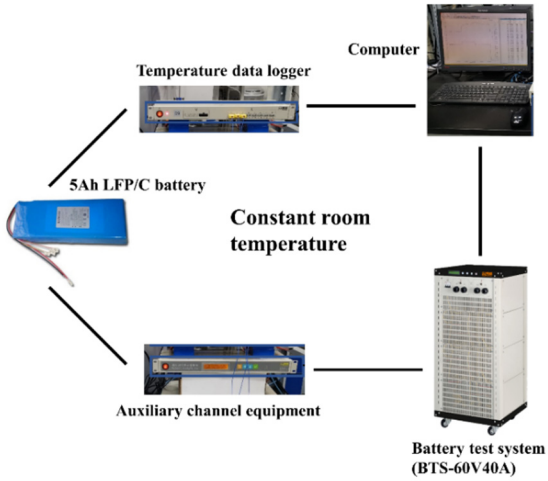

Figure 5. Schematic diagram of the experimental setup.

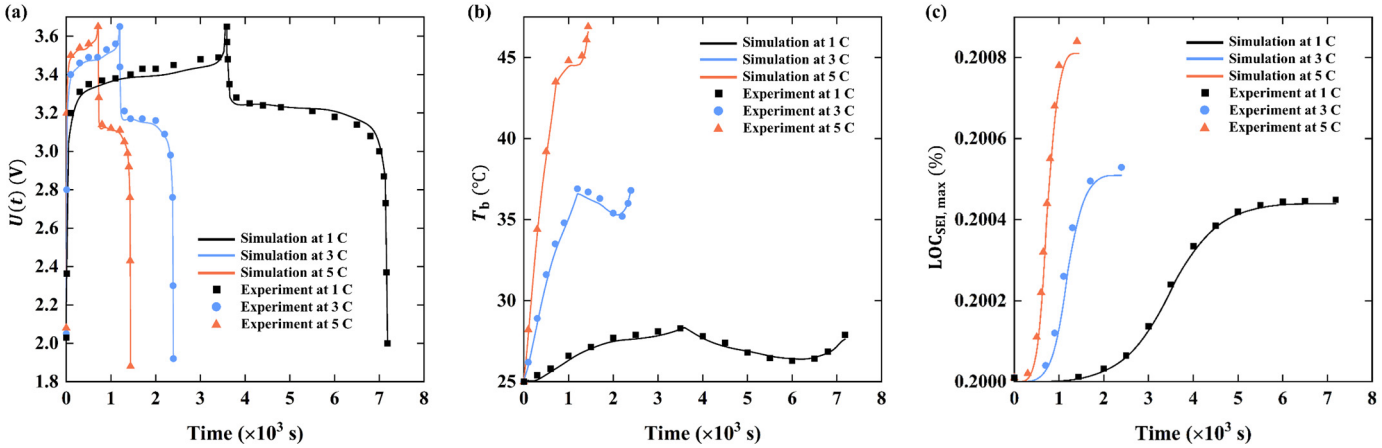

Figure 6. Comparison of voltage, temperature, and capacity fading in simulations and experiments: (**a**) voltage comparison at different C-rates; (**b**) temperature comparison at different C-rates; and (**c**) comparison of decrease in capacity at different C-rates.

4. Results and Discussion

4.1. Performance of Battery Cell and 6s4p Battery Pack under Natural Cooling

The thermal behavior and aging performance of a battery cell and the 6s4p battery pack were first investigated under natural cooling. The charge–discharge process of a single cell was first charged and then discharged and cycled at different C-rates and ambient temperatures (T_{amb}). The temperature and LOC evolutions of a single cell are shown in Figure 7. Taking the time required for one charge–discharge cycle at one C-rate as the standard, Figure 7a,b shows the battery temperature and LOC at C-rates from one to five. As the C-rate increases, the time for a single charge–discharge cycle becomes shorter, so the number of cycles increases. It can be observed that both the battery temperature and LOC increase with the increase in the C-rate. The maximum battery temperature can even exceed 50 °C at a C-rate of five, which is essentially consistent with the results of our previous research [32]. The LOC continues to increase as the charge–discharge cycles proceed, and

also correspondingly increases with the increasing C-rate. The initial LOC is 0.01 A·h, accounting for 0.2%. The final LOC exceeds 0.21% at a C-rate of five, which means that the newly added LOC reaches 0.01% after only about five charge–discharge cycles. For a C-rate of five, the evolutions of battery temperature and LOC at different T_{amb} are presented, as shown in Figure 7c,d. Both the battery temperature and LOC increase when the T_{amb} increases from 25 °C to 65 °C. The maximum battery temperature and LOC can even reach 80 °C and 1% at T_{amb} = 65 °C, respectively. A thermal runaway can occur in a battery cell when the temperature exceeds 80 °C, which is beyond the scope of this study. Therefore, both the C-rate and T_{amb} are critical for the thermal behavior and aging performance of a battery cell.

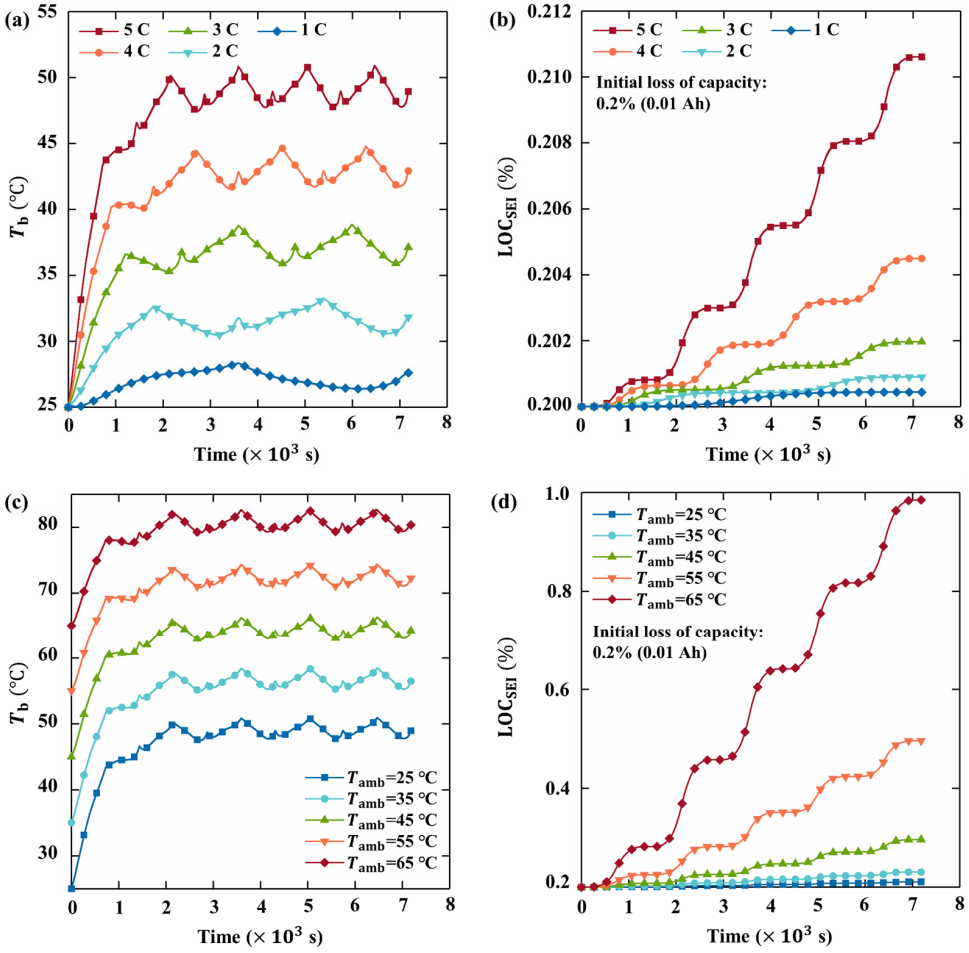

Figure 7. Evolutions of the temperature and LOC of a single battery: (**a**) battery temperature at different C-rates; (**b**) LOC at different C-rates; (**c**) battery temperature at different T_{amb} when C-rate is 5; (**d**) LOC at different T_{amb} when C-rate is 5.

Before studying the thermal behavior and aging performance of the 6s4p battery pack, the temperature and aging performance of a single cell are further summarized and analyzed. The temperature, LOC, SEI layer thickness, and SEI layer porosity of a single battery at different C-rates and ambient temperatures are shown in Figure 8. As shown in the figures, the C-rate plays an important role in the thermal behavior during the charge–discharge process of the battery cell. Moreover, the temperature rise is relatively uniform with the T_{amb} increasing from 25 °C to 65 °C, regardless of the C-rate. This indicates that although the battery temperature is greatly affected by the T_{amb}, the difference in the effect under different C-rates is small, as shown in Figure 8a. However, this situation is not the same for the aging performance of the battery cell, as shown in Figure 8b–d. As the C-rate and T_{amb} increase, the uptrend of LOC, SEI layer thickness, and SEI layer porosity is

slow at first and then sharp. It reveals that the high C-rate and T_{amb} extensively accelerate the battery aging, while normal C-rate and T_{amb} have less effect. Since the initial LOC is considered to be 0.2% (0.01 A·h), the initial SEI layer thickness and porosity are, 4.03848 nm and 0.01, respectively.

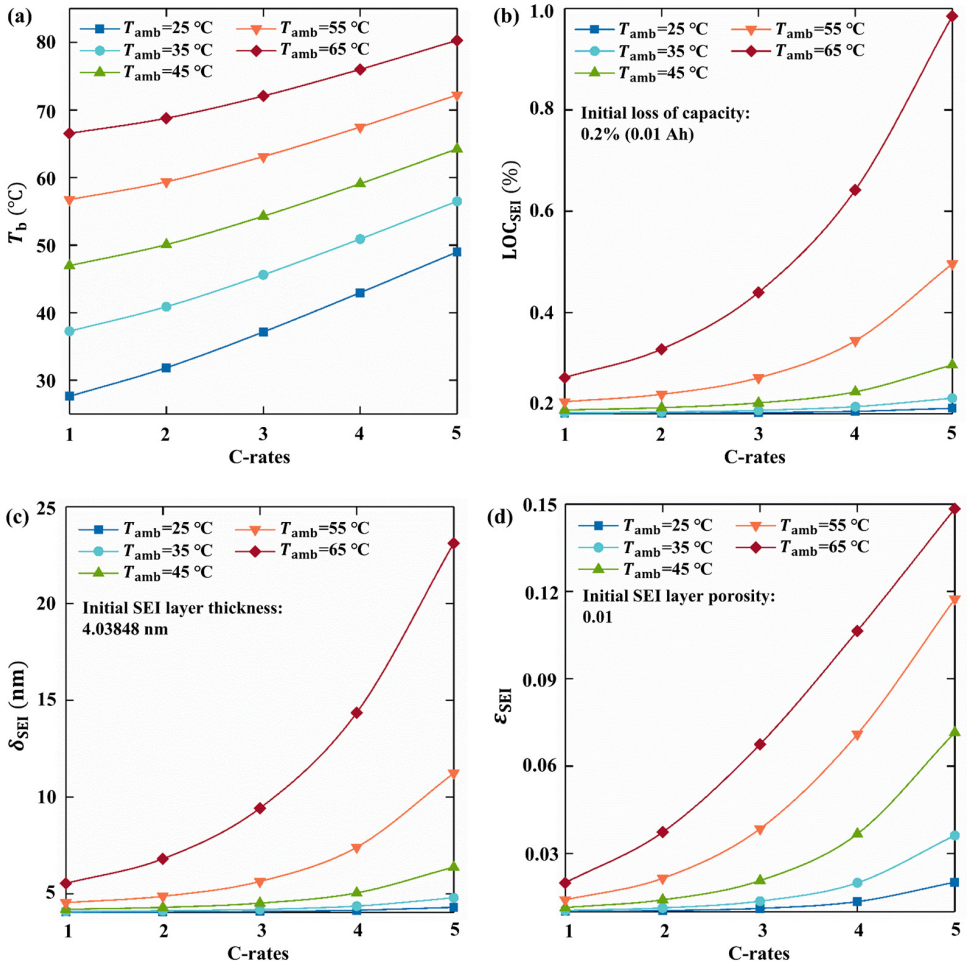

Figure 8. The temperature, LOC, SEI layer thickness, and SEI layer porosity of a single battery: (**a**) battery temperature at different C-rates and T_{amb}; (**b**) LOC at different C-rates and T_{amb}; (**c**) SEI layer thickness at different C-rates and T_{amb}; (**d**) SEI layer porosity at different C-rates and T_{amb}.

Based on the above analysis, the thermal behavior and aging performance of the 6s4p battery under natural cooling are then studied. The heat conduction between battery cells and heat convection and radiation between the cell and ambient air are considered. The evolutions of maximum battery temperature, LOC, SEI layer thickness, and SEI layer porosity in the 6s4p battery pack at T_{amb} = 25 °C are shown in Figure 9. The maximum battery temperature in the 6s4p battery pack can reach 80 °C at 5 C-rate, even if the T_{amb} is only 25 °C, as shown in Figure 9a. This means that the rapid heat generation of the battery pack at a high C-rate leads to a sharp increase in temperature, which requires the intervention of a thermal management system for timely cooling and heat dissipation. In addition, the SEI formation continuously occurs, resulting in the continuous increase of SEI layer thickness and porosity, and thus the LOC of the battery. Specifically, the maximum and minimum temperature, LOC, SEI layer thickness, and SEI layer porosity of the cells in the 6s4p battery pack at different C-rates are shown in Figure 10. As shown in the figures, squares of different styles and colors represent different meanings. Where green represents the initial value, red represents the maximum value, and blue represents the minimum value. The increase of the C-rate has a linear effect on the battery temperature, while the effect on the aging performance has a sudden change. The aging at low C-rates is small or

even negligible (such as 1 C and 2 C), but the aging at high C-rates is not negligible (such as 4 C and 5 C).

4.2. Performance of 6s4p Battery Pack under Two Modes Cooling System

After exploring the performance of the 6s4p battery pack under natural cooling, the thermal behavior and aging performance of the 6s4p battery pack in two cooling modes are further investigated and compared. For both parallel and series cooling, the pump rotary speeds of 1000 and 3000 r·min^{-1} are considered to provide the kinetic energy for coolant. According to the pump performance in the AMESim, the corresponding mechanical power provided by the pump to the coolant is 7.168 W and 218.873 W, and 2.620 W and 81.552 W under parallel and series cooling, respectively, as shown in Table 7. This indicates that parallel cooling is more energy efficient while series cooling requires a higher pump rotary speed to obtain the power. Further, the volumetric flow rate and velocity of the coolant can be obtained. It is worth mentioning that the flow in the four cold plates is the same under parallel cooling, which means a quarter of the total flow rate in each cold plate, as shown in Table 7. Therefore, for parallel cooling, the mass flow rates of each cold plate are, respectively, 0.081 and 0.276 kg·s^{-1} when the pump rotary speeds are 1000 and 3000 r·min^{-1}. For series cooling, the mass flow rates of each cold plate are always, respectively, 0.118 and 0.408 kg·s^{-1}. Combining the C-rates from 1 to 5, 20 cases (cases A to T) can be divided, as shown in Table 7.

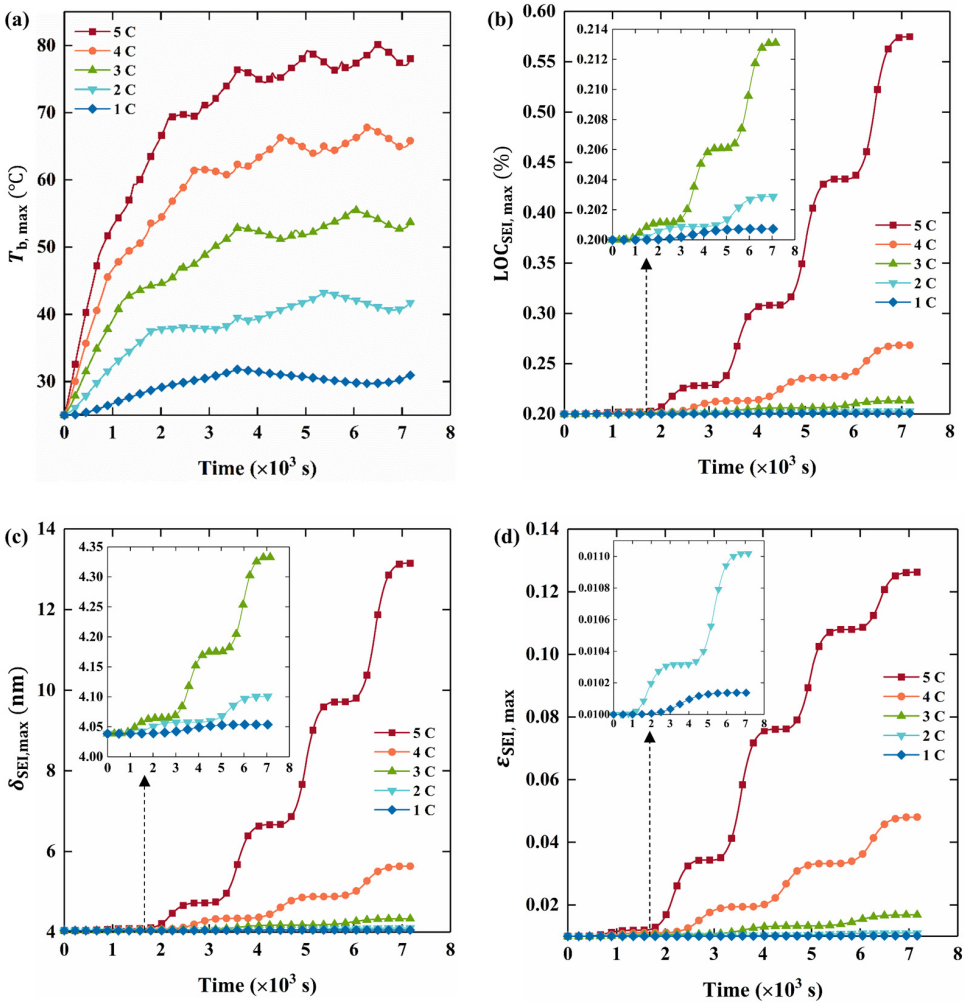

Figure 9. Evolutions of the maximum temperature, LOC, SEI layer thickness, and SEI layer porosity of the cells in the 6s4p battery pack at different C-rates: (**a**) the maximum temperature; (**b**) the maximum LOC; (**c**) the maximum SEI layer thickness; (**d**) the maximum SEI layer porosity.

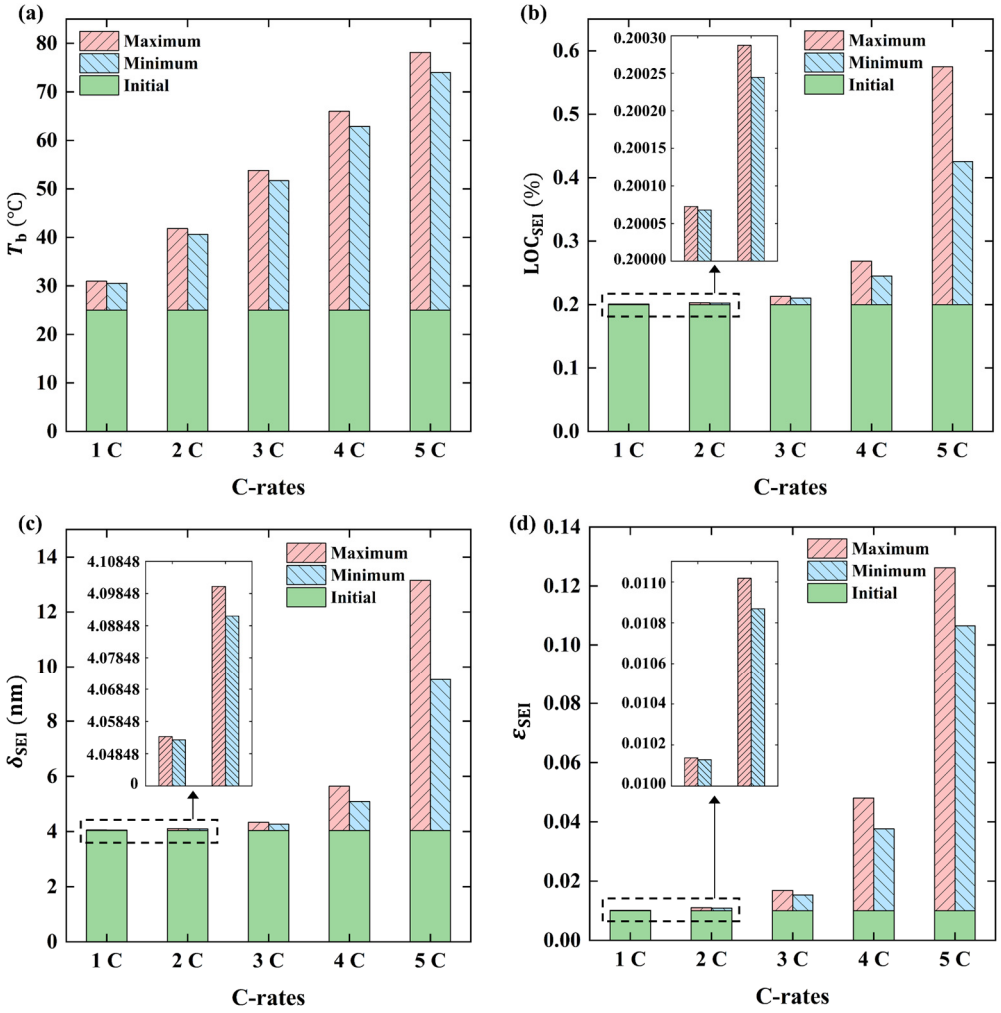

Figure 10. The maximum and minimum temperature, LOC, SEI layer thickness, and SEI layer porosity of the cells in the 6s4p battery pack at different C-rates: (**a**) the maximum and minimum temperature; (**b**) the maximum and minimum LOC; (**c**) the maximum and minimum SEI layer thickness; (**d**) the maximum and minimum SEI layer porosity.

Figure 11a,b show the evolutions of the maximum battery temperature in the 6s4p battery pack for the 20 cases. For both parallel and series cooling, the ambient temperature is set to 25 °C. Overall, under the same C-rate and coolant flow rate, the maximum battery temperature of the series and parallel cooling systems is close. From the specific values obtained from the simulation, the maximum battery temperature in the series connection is slightly higher. In addition, it is noteworthy that the maximum battery temperature in the 6s4p battery pack does not always decrease with the coolant flow rate increases. This phenomenon is particularly evident in parallel cooling, as shown in Figure 11a. When the C-rate is high, such as 4 C and 5 C, the heat generation of the battery is higher. A Larger coolant flow rate allows for faster heat exchange and more heat removal. Therefore, the maximum battery temperature at a higher coolant flow rate (Case F and G) is lower than that at a lower coolant flow rate (Case A and B). The opposite situation occurs when the C-rate is low, such as 1 C and 2 C. The battery does not generate much heat at this time, and a smaller coolant flow rate can carry out heat exchange for a longer time. Therefore, the maximum battery temperature at a lower coolant flow rate (Case D and E) is lower than that at a higher coolant flow rate (Case I and J). Further, the evolutions of the maximum temperature difference in the 6s4p battery pack for the 20 cases, as shown in Figure 11c,d. It can be observed that the maximum temperature difference in the 6s4p battery pack decreases with the coolant flow rate increasing, regardless of the C-rate. As the coolant

flow rate increases, the maximum temperature difference decreases more with parallel cooling than that with series cooling. This indicates that increasing the coolant flow rate can better reduce the temperature difference between the cells in the battery pack when parallel cooling is used. These results also demonstrate that at a high C-rate, a further increase in the coolant flow rate is required to control the temperature and temperature difference of the battery pack. Furthermore, parallel cooling is relatively more advantageous.

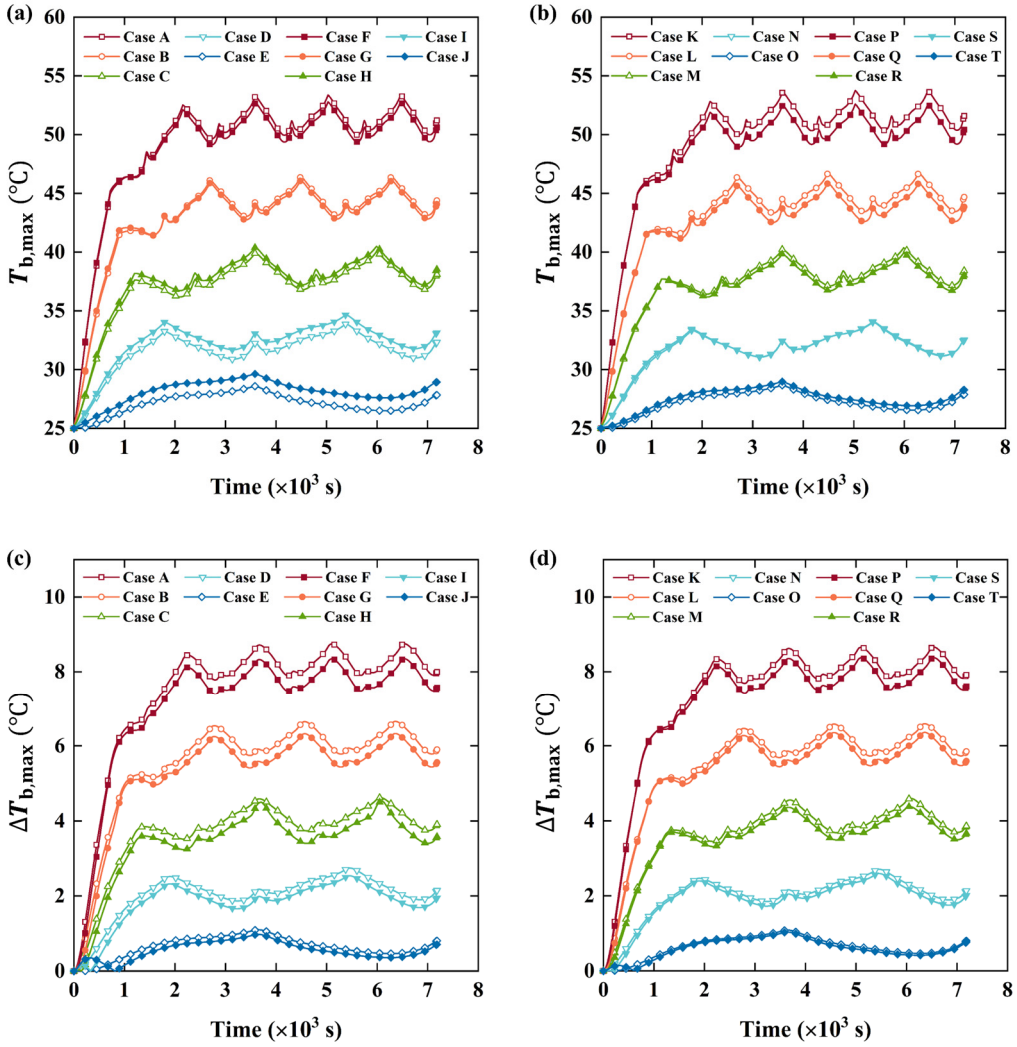

Figure 11. Evolutions of the maximum temperature and maximum temperature difference of the cells in the 6s4p battery pack at different conditions: (**a**) the maximum temperature under parallel cooling; (**b**) the maximum temperature under series cooling; (**c**) the maximum temperature difference under parallel cooling; (**d**) the maximum temperature difference under series cooling.

Based on the above analysis, the temperature, LOC, SEI layer thickness, and SEI layer porosity of the cells in the 6s4p battery pack under parallel cooling are further analyzed. After the charge–discharge process, the maximum and minimum battery temperatures at high and low coolant flow rates are calculated at different C-rates, as shown in Figure 12a. For high C-rates (4 C and 5 C), the maximum and minimum temperature at a higher coolant flow rate (0.276 kg·s^{-1}) is lower than those at a lower coolant flow rate (0.081 kg·s^{-1}). For low C-rates (1 C and 2 C), the maximum and minimum temperatures at a higher coolant flow rate are higher than those at a lower coolant flow rate. These results also validate the results in Figure 11. Further, the characteristics of this change caused by the difference in C-rate and coolant flow rate are also reflected in the parameters of battery aging, as shown in Figure 12b–d. The use of a higher coolant flow rate at high C-rates can not only reduce

the maximum temperature of the battery pack but also reduce the formation of SEI, thereby reducing capacity loss. Moreover, applying a higher coolant flow rate at low C-rates, not only is the optimization of battery temperature and aging performance not as good as those at a lower coolant flow rate, but a higher coolant flow rate also consumes more pump power. Therefore, high coolant flow is required at high C-rates, and low coolant flow is more suitable at low C-rates. All these show that it is necessary to select the appropriate coolant flow to ensure the performance of the battery. This requires timely adjustment of the coolant flow rate according to the working conditions of the battery.

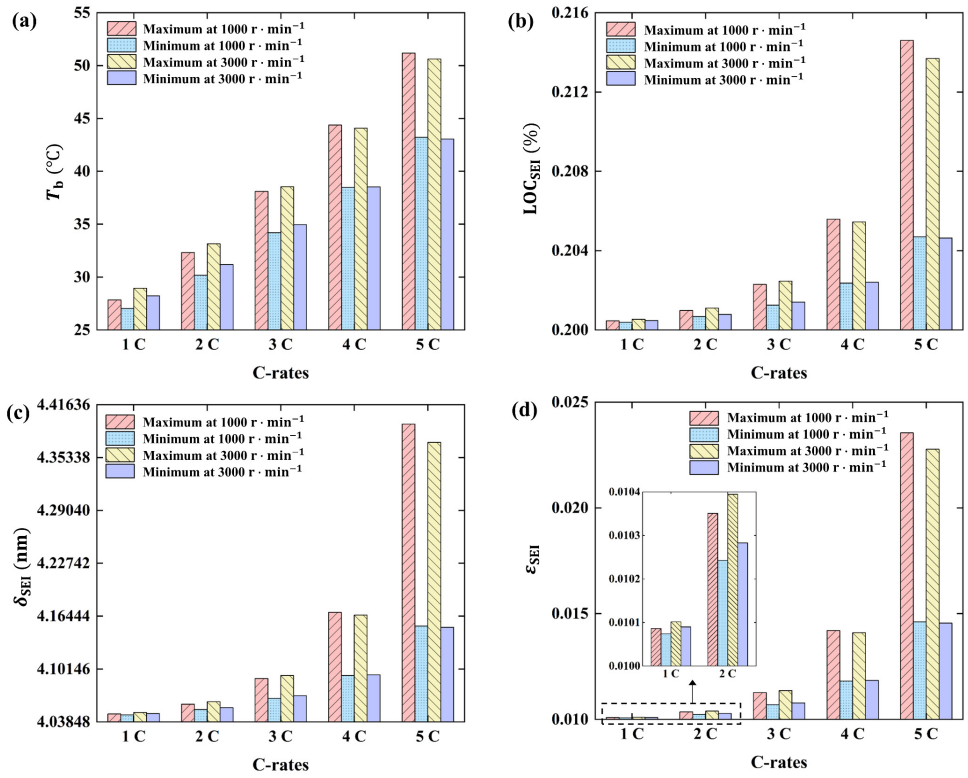

Figure 12. The temperature, LOC, SEI layer thickness, and SEI layer porosity of the cells in the 6s4p battery pack under parallel cooling: (**a**) battery temperature; (**b**) LOC; (**c**) SEI layer thickness; (**d**) SEI layer porosity.

4.3. Cooling Optimization of 6s4p Battery Pack under Different Cycle Conditions

As mentioned above, the triple-step nonlinear cooling control strategy is first solved for a single cell, and then this strategy is applied to the 6s4p battery pack to validate its applicability. Moreover, an extended PID cooling control strategy is also adopted to compare the results with those using a triple-step nonlinear cooling control strategy. Both the triple-step nonlinear method and the extended PID method adjust the temperature by changing the coolant flow rate. The effect of two methods is verified under constant current (2 C-rate), New European Driving Cycle (NEDC), and Urban Severe Driving Cycle (US06). Each working condition circulates two times to test the effect of control and optimization. NEDC consists of 4 urban cycles and 1 suburban cycle, and US06 represents an aggressive driving cycle. The initial temperature of the 6s4p battery pack is 40 °C, and the temperature of coolant and ambient is 25 °C.

Under 2 C-rate charge–discharge cycles, the heat generation of each battery cell is shown in Figure 13a. It can be seen that the heat generation in the discharge process is higher than that in the charging process. At the end of the charge and discharge process, the heat generation increases sharply. The well-tuned four parameters of the extended PID method are: $K_{ip} = 2 \times 10^{-4}$ (inner proportional element), $K_p = 6 \times 10^{-2}$ (proportional element), $K_i = 2 \times 10^{-6}$ (integral element), $K_d = 1 \times 10^{-4}$ (derivative element). The

comparison of coolant velocity under extended PID and triple-step nonlinear control is shown in Figure 13b. The coolant velocity increases continuously as the charge–discharge proceeds under the extended PID control, while under the triple-step nonlinear control, the coolant velocity increases smoothly. This indicates less pump power under the triple-step nonlinear control. The temperature comparison of battery 6, battery 5, and cold plate under extended PID and triple-step nonlinear control is shown in Figure 13c. As can be seen from the figure, under the triple-step nonlinear control, the temperature of the cold plate can be controlled at about 25 °C in a short time, while the extended PID control takes a little more time, which verifies the validity of the triple-step nonlinear method. Further, through the temperature evolution of batteries 5 and 6, the application effect of the two control methods in the 6s4p battery pack can be analyzed. The temperature of batteries 6 and 5 can be controlled to be below 35 °C and 32 °C in about 10 min, respectively. Although the subsequent charge–discharge process causes some temperature fluctuations, the temperature of batteries 6 and 5 can still be controlled below 34 °C and 31 °C, respectively. In addition, whether it is the temperature of the battery or the cold plate, the difference between the two methods is small, and the triple-step nonlinear method has a slight advantage. This slight advantage can be inferred from the aging performance of the batteries, as shown in Figure 13d. The LOC of batteries 6 and 5 under triple-step nonlinear control is smaller than that under the extended PID control.

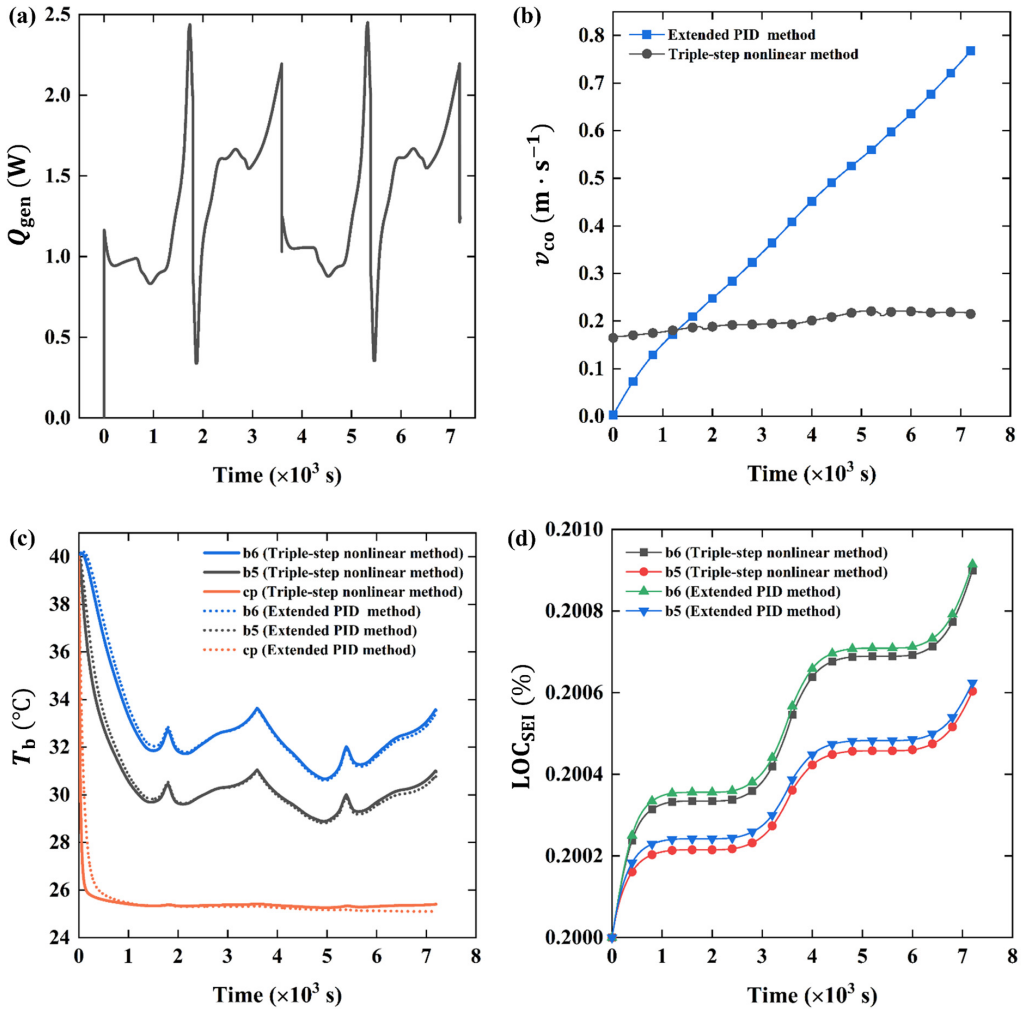

Figure 13. Parameters evolutions of key batteries at 2 C-rate: (**a**) heat generation of battery; (**b**) comparison of coolant velocity under extended PID and triple-step nonlinear control; (**c**) comparison of battery temperature under extended PID and triple-step nonlinear control; (**d**) comparison of LOC under extended PID and triple-step nonlinear control.

Under NEDC cycles, the heat generation of each battery cell is shown in Figure 14a. The heat generation also increases dramatically at the end of each urban and suburban cycle. The well-tuned four parameters of the extended PID method are: $K_{ip} = 3 \times 10^{-3}$, $K_p = 1 \times 10^{-2}$, $K_i = 2 \times 10^{-8}$, $K_d = 1 \times 10^{-4}$. The comparison of coolant velocity under extended PID and triple-step nonlinear control is shown in Figure 14b. The coolant velocity increases continuously under the extended PID control, while under the triple-step nonlinear control, the coolant velocity correspondingly changes with the change of heat generation. This indicates a more efficient control of coolant flow rate and less pump power consumption under the triple-step nonlinear control. The temperature comparison of battery 6, battery 5, and the cold plate is also shown in Figure 14c. The triple-step nonlinear method still shows a good control effect on the temperature of the cold plate. The temperature of batteries 6 and 5 can be controlled to be below 34 °C and 32 °C in about 6 min, respectively. During the subsequent cycle, the temperature of batteries 6 and 5 can further be controlled to be below 29 °C and 28 °C, respectively. The triple-step nonlinear method still has a slight advantage, which can be inferred from the aging performance of the batteries, as shown in Figure 14d.

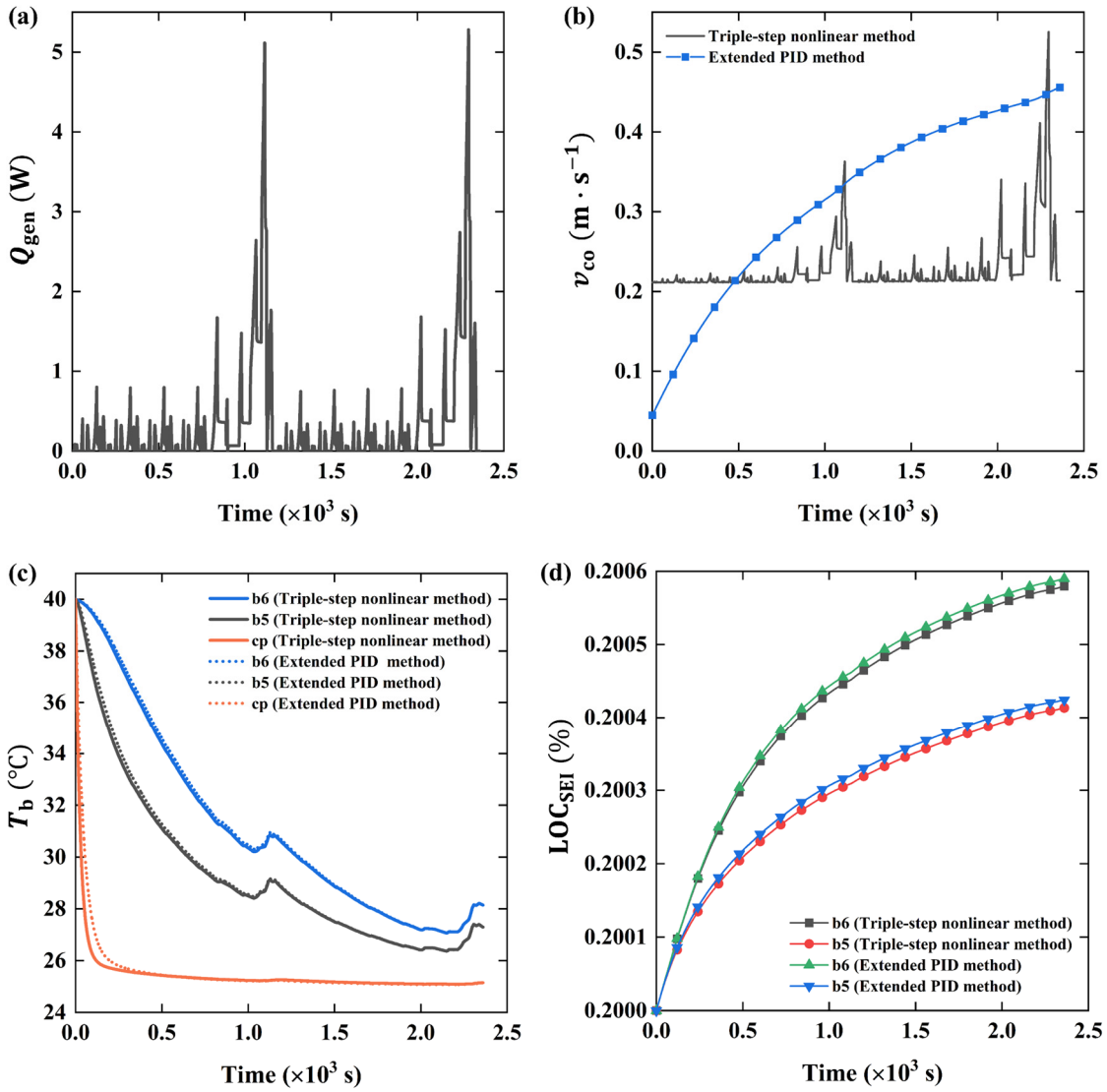

Figure 14. Parameters evolutions of key batteries under NEDC: (**a**) heat generation of battery; (**b**) comparison of coolant velocity under extended PID and triple-step nonlinear control; (**c**) comparison of battery temperature under extended PID and triple-step nonlinear control; (**d**) comparison of LOC under extended PID and triple-step nonlinear control.

Under US06 cycles, the heat generation of each battery cell is shown in Figure 15a. The aggressive driving cycles lead to dramatic and fluctuating heat generation. The well-tuned four parameters of the extended PID method are: $K_{ip} = 3 \times 10^{-3}$, $K_p = 1.5 \times 10^{-2}$, $K_i = 2 \times 10^{-7}$, $K_d = 1 \times 10^{-4}$. The comparison of coolant velocity under extended PID and triple-step nonlinear control is shown in Figure 15b. The coolant velocity still increases continuously under the extended PID control, while under the triple-step nonlinear control, the coolant velocity correspondingly fluctuates with the change of the heat generation. This also indicates a more efficient control of coolant flow rate and less pump power consumption under the triple-step nonlinear control. The temperature comparison of battery 6, battery 5, and the cold plate is also shown in Figure 15c. The triple-step nonlinear method still shows a good control effect on the temperature of the cold plate. The temperature of batteries 6 and 5 can be controlled to be below 38 °C and 34 °C in about 9 min, respectively. During the subsequent cycle, the temperature of batteries 6 and 5 can further be controlled to be below 36 °C and 32 °C, respectively. The triple-step nonlinear method still has a slight advantage, which can be inferred from the aging performance of the batteries, as shown in Figure 15d.

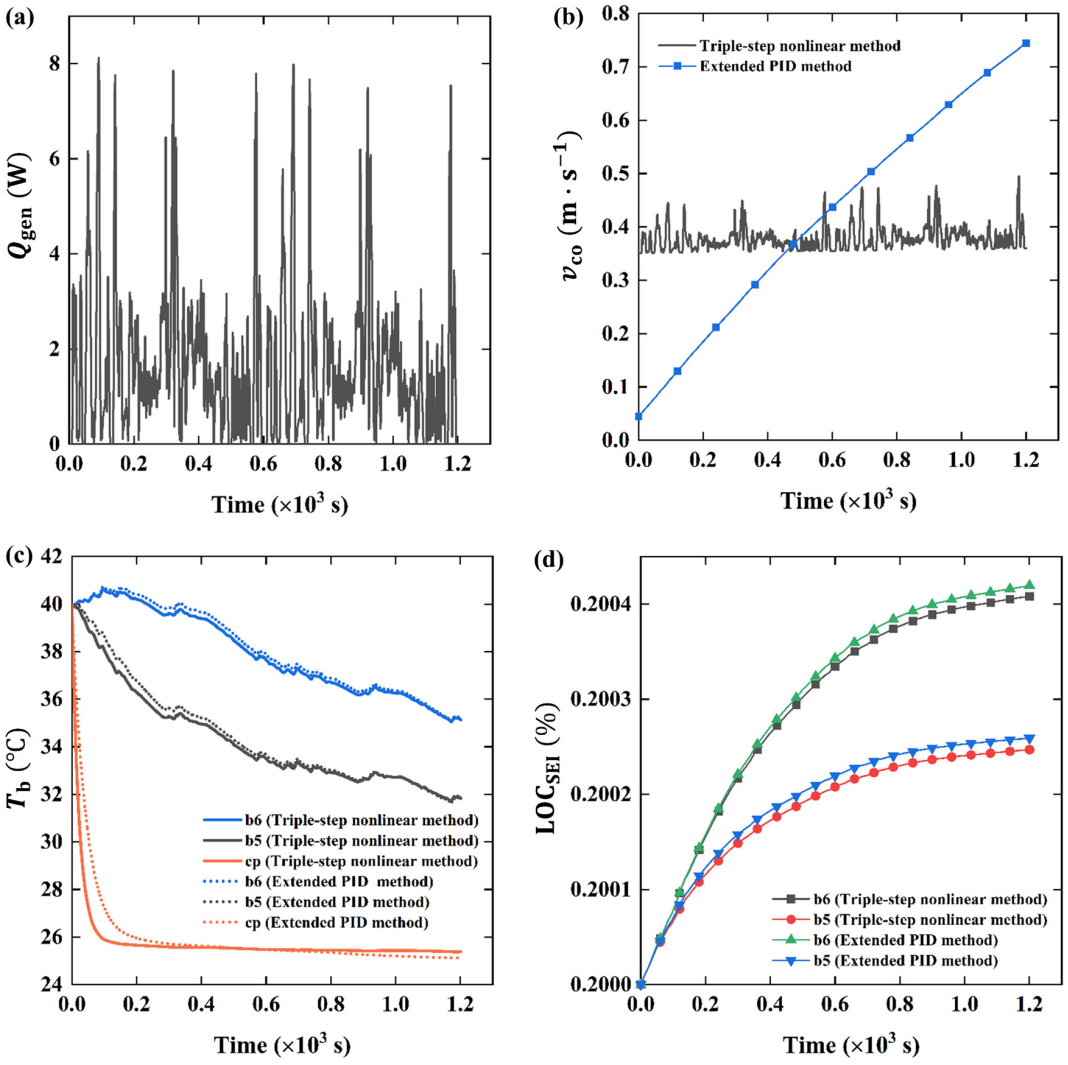

Figure 15. Parameters evolutions of key batteries under US06: (**a**) heat generation of battery; (**b**) comparison of coolant velocity under extended PID and triple-step nonlinear control; (**c**) comparison of battery temperature under extended PID and triple-step nonlinear control; (**d**) comparison of LOC under extended PID and triple-step nonlinear control.

5. Conclusions

Two modes of thermal management system for 6s4p battery pack are established based on one-dimensional modeling. The single particle model with the consideration of aging is adopted for the battery. Both the battery temperature and loss of capacity (LOC) increase when the C-rate and ambient temperature (T_{amb}) increase. The maximum battery temperature and LOC can even reach 80 °C and 1% at T_{amb} = 65 °C, respectively. High C-rate and T_{amb} can extensively accelerate the battery aging, while normal C-rate and T_{amb} have weaker effect. The maximum battery temperature in the 6s4p battery pack can reach 80 °C at 5 C-rate, even if the T_{amb} is only 25 °C. The comparison of pump power, thermal behavior, and aging performance indicate parallel cooling is relatively more advantageous. When the C-rate is high (4 C and 5 C), the maximum battery temperature at a higher coolant flow rate (0.276 kg·s^{-1}) is lower than that at a lower coolant flow rate (0.081 kg·s^{-1}). When the C-rate is low (1 C and 2 C), the maximum battery temperature at a lower coolant flow rate is lower than that at a higher coolant flow rate. The characteristics of this change caused by the difference in C-rate and coolant flow rate are also reflected in the battery aging. Further, a cooling control strategy for the key battery is firstly proposed based on the triple-step nonlinear method, and then the optimization effect of this strategy in the battery pack is validated under 2 C charge–discharge cycles, NEDC cycles, and US06 cycles. Moreover, the extended PID control strategy is constructed and compared with the triple-step nonlinear method. The results show that the temperature and LOC of key batteries and the temperature of the cold plate are lower than that of the extended PID method. This verifies the validity of the triple-step nonlinear method and shows an advantage compared with the extended PID method.

Author Contributions: Conceptualization, H.Z.; methodology, H.Z.; software, H.Z. and H.C.; validation, H.Z. and H.C.; formal analysis, H.Z., H.C. and H.F.; investigation, H.Z.; resources, H.F.; data curation, H.C.; writing—original draft preparation, H.Z.; writing—review and editing, H.Z., H.C. and H.F.; funding acquisition, H.F.; All authors have read and agreed to the published version of the manuscript.

Funding: This research received no external funding.

Data Availability Statement: The data that support the findings of this study are available from the corresponding author upon reasonable request.

Conflicts of Interest: The authors declare no conflict of interest.

Nomenclature

Q_{tra}	Heat transferred from the battery to the ambient (W)
h_{conv}	Convective heat transfer coefficient (W·m^{-2}·K^{-1})
A_b	Contact area between the battery and the ambient air (m^2)
T_b	Battery temperature (K)
T_{amb}	Ambient temperature (K)
S_p	Active area of positive electrode (m^2)
S_{sep}	Active area of separator (m^2)
S_n	Active area of negative electrode (m^2)
A_{ele}	Active area of electrode (m^2)
I	Electric current (A)
k_b	Thermal conductivity of battery (W·m^{-1}·K^{-1})
$C_{p,b}$	Specific thermal capacity of battery (J·kg^{-1}·K^{-1})
U_p	Thermodynamic potential of the positive electrode (V)
U_n	Thermodynamic potential of the negative electrode (V)
z	Battery thickness direction
$c^b_{s,p}$	Bulk Li concentration in the solid phase for positive electrode (mol·m^{-3})
$c^b_{s,n}$	Bulk Li concentration in the solid phase for negative electrode (mol·m^{-3})
u_e	Error feedback control law
e	Input error
Greek symbols	
χ	Surface emissivity
σ_B	Stefan-Boltzmann constant
ρ_b	Density of battery (kg·m^{-3})
$\eta(L)$	Overpotential at $z = L$
$\eta(0)$	Overpotential at $z = 0$
$\phi_e(L)$	Electrolyte potential at $z = L$
$\phi_e(0)$	Electrolyte potential at $z = 0$
ψ	Hysteresis factor
ε_e	Volume fraction of electrolyte
σ^{eff}	Effective solid phase conductivity (S·m^{-1})
ϕ_s	Potential of solid phase (V)
κ^{eff}	Electrolyte effective ionic conductivity (S·m^{-1})
κ^{eff}_D	Electrolyte effective ionic conductivity (S·m^{-1})
α_{ox}	Charge transfer coefficient of the anodic reaction

$c_{s,p}^{max}$	Maximum Li concentration in the positive electrode ($mol \cdot m^{-3}$)
$c_{s,n}^{max}$	Maximum Li concentration in the negative electrode ($mol \cdot m^{-3}$)
U_p^{ref}	Reference potential of the positive electrode (V)
U_n^{ref}	Reference potential of the negative electrode (V)
f_{ts}	Transition factor
x	Insertion rate
$U_p^{ch,ref}$	Charge reference potentials of the positive electrode (V)
$U_p^{dch,ref}$	Discharge reference potentials of the positive electrode (V)
$U_n^{ch,ref}$	Charge reference potentials of the negative electrode (V)
$U_n^{dch,ref}$	Discharge reference potentials of the negative electrode (V)
T_{ref}	Reference temperature
c_s	Li concentration in the active material particles ($mol \cdot m^{-3}$)
r	Radial coordinate inside a spherical particle (m)
D_s	Solid phase diffusion coefficient ($m^2 \cdot s^{-1}$)
j_f	Current per volume unit ($A \cdot m^{-3}$)
a_s	Specific interfacial surface area (m^{-1})
F	Faraday constant ($C \cdot mol^{-1}$)
c_e	Concentration of the electrolyte ($mol \cdot m^{-3}$)
D_e^{eff}	Effective electrolyte phase diffusion coefficient ($m^2 \cdot s^{-1}$)
t_+	Lithium transference number
L_{NE}	Thickness of the positive electrode
L_{PE}	Thickness of the negative electrode
i_0	Exchange current density (A)
R	Ideal gas constant
T	Temperature
D_e	Electrolyte phase diffusion coefficient ($m^2 \cdot s^{-1}$)
k_0	Reaction rate constant ($m^{2.5} \cdot mol^{-0.5} \cdot s^{-1}$)
$f_\pm$	Electrolyte activity coefficient
R_s	Radius of spherical particle (m)
$c_{s,p}^{R_{s,p}}$	Li concentration at the positive electrode-electrolyte interface phase ($mol \cdot m^{-3}$)
$c_{s,n}^{R_{s,n}}$	Li concentration at the negative electrode-electrolyte interface phase ($mol \cdot m^{-3}$)
F	Faraday constant
j_{SEI}	Parasitic current density for SEI layer formation ($A \cdot m^{-2}$)
k_{SEI}	SEI formation reaction constant ($m^7 \cdot mol^{-2} \cdot K^{-1}$)
$c_{solv}^{partedg}$	Concentration of the solvent at the particle edge ($mol \cdot m^{-3}$)
U_{SEI}	Solvent reduction potential of the SEI layer (V)
c_{solv}	Concentration of the solvent ($mol \cdot m^{-3}$)
D_{solv}	SEI layer solvent diffusivity ($m^2 \cdot s^{-1}$)
c_{solv}^b	Bulk concentration of the solvent ($mol \cdot m^{-3}$)
C_{loss}^{SEI}	Cycling lithium loss due to SEI formation (A·h)
LOC_{SEI}	Loss of capacity due to SEI formation
C_{tot}	Total capacity (A·h)
M_{SEI}	SEI molar mass ($kg \cdot mol^{-3}$)
$x_{n,0}$	Negative insertion rate when the state of charge is zero
C_{nom}	Nominal capacity (A·h)
m_b	Mass of the battery (kg)
j_{tot}	Total current intensity ($A \cdot m^{-3}$)
Q_{gen}	Generated heat of battery (W)
Q_{b5-co}	Heat transferred from cell 5 to coolant (W)
h_{b5-co}	Heat transfer coefficient between cell 5 and coolant ($W \cdot m^{-2} \cdot K^{-1}$)
A_{b5-co}	Contact area between cell 5 and coolant (m^2)
Nu_{co}	Nusselt number of the coolant
Re_{co}	Reynolds number of the coolant
Pr_{co}	Prandtl number of the coolant
v_{co}	Flow velocity of the coolant ($m \cdot s^{-1}$)
u_s	Steady-state-like control law
u_f	Reference variable feed-forward control law
α_{red}	Charge transfer coefficient of the reduction reaction
η	Overpotential (V)
γ_e	Electrolyte Bruggeman exponent
σ	Solid phase conductivity
ε_s	Volume fraction of the active material
η_p^{diff}	Solid phase overpotential of positive electrode (V)
η_n^{diff}	Solid phase overpotential of negative electrode (V)
$\eta_{s,p}^{ohm}$	Solid ohmic overpotential of positive electrode (V)
$\eta_{s,n}^{ohm}$	Solid ohmic overpotential of negative electrode (V)
η_e^{diff}	Electrolyte diffusion overpotential (V)
η_e^{ohm}	Electrolyte ohmic overpotential (V)
β_{SEI}	Reaction charge transfer coefficient of the SEI layer formation
δ_{SEI}	SEI layer thickness (m)
κ_{SEI}	SEI layer conductivity ($S \cdot m^{-1}$)
ε_{SEI}	SEI layer porosity
ε_{SEI}^*	Instantaneous formed SEI layer porosity
ρ_{SEI}	SEI layer density ($kg \cdot m^{-3}$)
η_{SEI}	SEI ohmic overvoltage (V)
$\kappa_{SEI,data}$	Index of the SEI layer electronic conductivity data ($S \cdot m^{-1}$)
γ_{SEI}	SEI Bruggeman exponent
$\varepsilon_{e,n}$	Porosity of the negative electrode
ρ_{co}	Density of the coolant ($kg \cdot m^{-3}$)
μ_{co}	Dynamic viscosity of the coolant (Pa·s)
μ_w	Dynamic viscosity near the wall in the pipe (Pa·s)

Subscripts and superscripts

conv	Convection
b	Battery
s	Solid phase
p	Positive electrode
n	Negative electrode
max	Maximum
e	Electrolyte
eff	Effective
diff	Difference
int	Initial
ir	Irreversible
r	Reversible
co	Coolant
tv	Target value
b5	Battery 5

Acronyms

EVs	Electric vehicles
LIBs	Lithium-ion batteries
BTM	Battery thermal management
NE	Negative electrode
PE	Positive electrode
SEI	solid electrolyte interface
SP	Single particle
LFP	Lithium iron phosphate
SOC	state of charge
AMESim	Advanced Modeling Environment for performing Simulation of engineering systems
NCC	Negative current collector
SEP	Separator
PCC	Positive current collector
LOC	Loss of capacity

References

1. Al-Zareer, M.; Dincer, I.; Rosen, M.A. A Review of Novel Thermal Management Systems for Batteries. *Int. J. Energy Res.* **2018**, *42*, 3182–3205. [CrossRef]
2. Patil, M.S.; Seo, J.H.; Panchal, S.; Jee, S.W.; Lee, M.Y. Investigation on Thermal Performance of Water-Cooled Li-Ion Pouch Cell and Pack at High Discharge Rate with U-Turn Type Microchannel Cold Plate. *Int. J. Heat Mass Transf.* **2020**, *155*, 119728. [CrossRef]
3. Panchal, S.; Gudlanarva, K.; Tran, M.K.; Fraser, R.; Fowler, M. High Reynold's Number Turbulent Model for Micro-Channel Cold Plate Using Reverse Engineering Approach for Water-Cooled Battery in Electric Vehicles. *Energies* **2020**, *13*, 1638. [CrossRef]
4. Ye, M.; Guo, H.; Xiong, R.; Yu, Q. A Double-Scale and Adaptive Particle Filter-Based Online Parameter and State of Charge Estimation Method for Lithium-Ion Batteries. *Energy* **2018**, *144*, 789–799. [CrossRef]
5. Tran, M.K.; Panchal, S.; Chauhan, V.; Brahmbhatt, N.; Mevawalla, A.; Fraser, R.; Fowler, M. Python-Based Scikit-Learn Machine Learning Models for Thermal and Electrical Performance Prediction of High-Capacity Lithium-Ion Battery. *Int. J. Energy Res.* **2022**, *46*, 786–794. [CrossRef]
6. Hekmat, S.; Molaeimanesh, G.R. Hybrid Thermal Management of a Li-Ion Battery Module with Phase Change Material and Cooling Water Pipes: An Experimental Investigation. *Appl. Therm. Eng.* **2020**, *166*, 114759. [CrossRef]
7. Li, L.; Chen, X.; Yuan, Q.; Wang, T.; Ji, H.; Papović, S.; Raleva, K.; Pan, F.; Yang, T.; Li, J. Effects of Minor Mechanical Deformation on the Lifetime and Performance of Commercial 21700 Lithium-Ion Battery. *J. Electrochem. Soc.* **2022**, *169*, 060544. [CrossRef]
8. Latini, D.; Vaccari, M.; Lagnoni, M.; Orefice, M.; Mathieux, F.; Huisman, J.; Tognotti, L.; Bertei, A. A Comprehensive Review and Classification of Unit Operations with Assessment of Outputs Quality in Lithium-Ion Battery Recycling. *J. Power Sources* **2022**, *546*, 231979. [CrossRef]
9. Ghaeminezhad, N.; Wang, Z.; Ouyang, Q. A Review on Lithium-Ion Battery Thermal Management System Techniques: A Control-Oriented Analysis. *Appl. Therm. Eng.* **2023**, *219*, 119497. [CrossRef]
10. Wu, W.; Wang, S.; Wu, W.; Chen, K.; Hong, S.; Lai, Y. A Critical Review of Battery Thermal Performance and Liquid Based Battery Thermal Management. *Energy Convers. Manag.* **2019**, *182*, 262–281. [CrossRef]
11. Kim, J.; Oh, J.; Lee, H. Review on Battery Thermal Management System for Electric Vehicles. *Appl. Therm. Eng.* **2019**, *149*, 192–212. [CrossRef]
12. Aswin Karthik, C.; Kalita, P.; Cui, X.; Peng, X. Thermal Management for Prevention of Failures of Lithium Ion Battery Packs in Electric Vehicles: A Review and Critical Future Aspects. *Energy Storage* **2020**, *2*, e137. [CrossRef]
13. Lin, J.; Liu, X.; Li, S.; Zhang, C.; Yang, S. A Review on Recent Progress, Challenges and Perspective of Battery Thermal Management System. *Int. J. Heat Mass Transf.* **2021**, *167*, 120834. [CrossRef]
14. Mohammadian, S.K.; Zhang, Y. Thermal Management Optimization of an Air-Cooled Li-Ion Battery Module Using Pin-Fin Heat Sinks for Hybrid Electric Vehicles. *J. Power Sources* **2015**, *273*, 431–439. [CrossRef]
15. Mohammadian, S.K.; Rassoulinejad-Mousavi, S.M.; Zhang, Y. Thermal Management Improvement of an Air-Cooled High-Power Lithium-Ion Battery by Embedding Metal Foam. *J. Power Sources* **2015**, *296*, 305–313. [CrossRef]
16. An, Z.; Shah, K.; Jia, L.; Ma, Y. A Parametric Study for Optimization of Minichannel Based Battery Thermal Management System. *Appl. Therm. Eng.* **2019**, *154*, 593–601. [CrossRef]
17. Liu, J.; Li, H.; Li, W.; Shi, J.; Wang, H.; Chen, J. Thermal Characteristics of Power Battery Pack with Liquid-Based Thermal Management. *Appl. Therm. Eng.* **2020**, *164*, 114421. [CrossRef]
18. Mortazavi, B.; Yang, H.; Mohebbi, F.; Cuniberti, G.; Rabczuk, T. Graphene or H-BN Paraffin Composite Structures for the Thermal Management of Li-Ion Batteries: A Multiscale Investigation. *Appl. Energy* **2017**, *202*, 323–334. [CrossRef]
19. Zhang, W.; Ling, G.; Zhuang, L.; Liang, Z. The Effect of Reducing the Thermal Contact Resistance on the Performance of Battery Thermal Management System. *Int. J. Energy Res.* **2021**, *45*, 9970–9982. [CrossRef]
20. Liu, F.F.; Lan, F.C.; Chen, J.Q.; Li, Y.G. Experimental Investigation on Cooling/Heating Characteristics of Ultra-Thin Micro Heat Pipe for Electric Vehicle Battery Thermal Management. *Chinese J. Mech. Eng.* **2018**, *31*, 53. [CrossRef]
21. Zhang, Z.; Wei, K. Experimental and Numerical Study of a Passive Thermal Management System Using Flat Heat Pipes for Lithium-Ion Batteries. *Appl. Therm. Eng.* **2020**, *166*, 114660. [CrossRef]
22. Li, X.; He, F.; Zhang, G.; Huang, Q.; Zhou, D. Experiment and Simulation for Pouch Battery with Silica Cooling Plates and Copper Mesh Based Air Cooling Thermal Management System. *Appl. Therm. Eng.* **2019**, *146*, 866–880. [CrossRef]
23. Dan, D.; Yao, C.; Zhang, Y.; Zhang, H.; Zeng, Z.; Xu, X. Dynamic Thermal Behavior of Micro Heat Pipe Array-Air Cooling Battery Thermal Management System Based on Thermal Network Model. *Appl. Therm. Eng.* **2019**, *162*, 114183. [CrossRef]
24. Zhang, L.; Yuan, Q.; Hu, S.; Xu, X. Research on Performance of Thermal Management System Integrated with Multiple Heat Exchange Methods. *Ionics* **2022**, *28*, 789–799. [CrossRef]
25. Kabir, M.M.; Demirocak, D.E. Degradation Mechanisms in Li-Ion Batteries: A State-of-the-Art Review. *Int. J. Energy Res.* **2017**, *41*, 1963–1986. [CrossRef]
26. Xiong, R.; Pan, Y.; Shen, W.; Li, H.; Sun, F. Lithium-Ion Battery Aging Mechanisms and Diagnosis Method for Automotive Applications: Recent Advances and Perspectives. *Renew. Sustain. Energy Rev.* **2020**, *131*, 110048. [CrossRef]
27. Birkl, C.R.; Roberts, M.R.; McTurk, E.; Bruce, P.G.; Howey, D.A. Degradation Diagnostics for Lithium Ion Cells. *J. Power Sources* **2017**, *341*, 373–386. [CrossRef]
28. Kamyab, N.; Weidner, J.W.; White, R.E. Mixed Mode Growth Model for the Solid Electrolyte Interface (SEI). *J. Electrochem. Soc.* **2019**, *166*, A334–A341. [CrossRef]

29. Yang, S.-c.; Hua, Y.; Qiao, D.; Lian, Y.-b.; Pan, Y.-w.; He, Y.-l. A Coupled Electrochemical-Thermal-Mechanical Degradation Modelling Approach for Lifetime Assessment of Lithium-Ion Batteries. *Electrochim. Acta* **2019**, *326*, 134928. [CrossRef]
30. Sun, S.; Guan, T.; Cheng, X.; Zuo, P.; Gao, Y.; Du, C.; Yin, G. Accelerated Aging and Degradation Mechanism of LiFePO4/Graphite Batteries Cycled at High Discharge Rates. *RSC Adv.* **2018**, *8*, 25695–25703. [CrossRef] [PubMed]
31. Liang, J.; Gan, Y.; Yao, M.; Li, Y. Numerical Analysis of Capacity Fading for a LiFePO4 Battery under Different Current Rates and Ambient Temperatures. *Int. J. Heat Mass Transf.* **2021**, *165*, 120615. [CrossRef]
32. Zhang, H.; Li, C.; Zhang, R.; Lin, Y.; Fang, H. Thermal Analysis of a 6s4p Lithium-Ion Battery Pack Cooled by Cold Plates Based on a Multi-Domain Modeling Framework. *Appl. Therm. Eng.* **2020**, *173*, 115216. [CrossRef]
33. An, Z.; Jia, L.; Wei, L.; Yang, C. Numerical Modeling and Analysis of Thermal Behavior and Li+ Transport Characteristic in Lithium-Ion Battery. *Int. J. Heat Mass Transf.* **2018**, *127*, 1351–1366. [CrossRef]
34. Zhao, P.; Li, M.; Kang, J.; Rizzoni, G. Analysis of Fading Characteristics of a Lithium Ion Battery Based on an Integration Model. *Int. J. Heat Mass Transf.* **2017**, *104*, 1317–1324. [CrossRef]
35. Dong, T.; Peng, P.; Jiang, F. Numerical Modeling and Analysis of the Thermal Behavior of NCM Lithium-Ion Batteries Subjected to Very High C-Rate Discharge/Charge Operations. *Int. J. Heat Mass Transf.* **2018**, *117*, 261–272. [CrossRef]
36. Haran, B.S.; Popov, B.N.; White, R.E. Determination of the Hydrogen Diffusion Coefficient in Metal Hydrides by Impedance Spectroscopy. *J. Power Sources* **1998**, *75*, 56–63. [CrossRef]
37. Fuller, T.F.; Doyle, M.; Newman, J. Simulation and Optimization of the Dual Lithium Ion Insertion Cell. *J. Electrochem. Soc.* **1994**, *141*, 1–10. [CrossRef]
38. Rahimian, S.K.; Rayman, S.; White, R.E. Comparison of Single Particle and Equivalent Circuit Analog Models for a Lithium-Ion Cell. *J. Power Sources* **2011**, *196*, 8450–8462. [CrossRef]
39. Li, J.; Adewuyi, K.; Lotfi, N.; Landers, R.G.; Park, J. A Single Particle Model with Chemical/Mechanical Degradation Physics for Lithium Ion Battery State of Health (SOH) Estimation. *Appl. Energy* **2018**, *212*, 1178–1190. [CrossRef]
40. Richardson, G.; Korotkin, I.; Ranom, R.; Castle, M.; Foster, J.M. Generalised Single Particle Models for High-Rate Operation of Graded Lithium-Ion Electrodes: Systematic Derivation and Validation. *Electrochim. Acta* **2020**, *339*, 135862. [CrossRef]
41. Ren, L.; Zhu, G.; Kang, J.; Wang, J.V.; Luo, B.; Chen, C.; Xiang, K. An Algorithm for State of Charge Estimation Based on a Single-Particle Model. *J. Energy Storage* **2021**, *39*, 102644. [CrossRef]
42. Ji, B.; Song, X.G.; Cao, W.P.; Pickert, V. Active Temperature Control of Li-Ion Batteries in Electric Vehicles. *IET Conf. Publ.* **2013**, *2013*, 3–7. [CrossRef]
43. Zhu, C.; Lu, F.; Zhang, H.; Mi, C.C. Robust Predictive Battery Thermal Management Strategy for Connected and Automated Hybrid Electric Vehicles Based on Thermoelectric Parameter Uncertainty. *IEEE J. Emerg. Sel. Top. Power Electron.* **2018**, *6*, 1796–1805. [CrossRef]
44. Ma, Y.; Mou, H.; Zhao, H. Cooling Optimization Strategy for Lithium-Ion Batteries Based on Triple-Step Nonlinear Method. *Energy* **2020**, *201*, 117678. [CrossRef]
45. Ma, Y.; Ding, H.; Mou, H.; Gao, J. Battery Thermal Management Strategy for Electric Vehicles Based on Nonlinear Model Predictive Control. *Meas. J. Int. Meas. Confed.* **2021**, *186*, 110115. [CrossRef]
46. Xu, M.; Zhang, Z.; Wang, X.; Jia, L.; Yang, L. Two-Dimensional Electrochemical-Thermal Coupled Modeling of Cylindrical LiFePO4 Batteries. *J. Power Sources* **2014**, *256*, 233–243. [CrossRef]
47. Kim, G.H.; Pesaran, A.; Spotnitz, R. A Three-Dimensional Thermal Abuse Model for Lithium-Ion Cells. *J. Power Sources* **2007**, *170*, 476–489. [CrossRef]
48. Li, C.; Zhang, H.; Zhang, R.; Lin, Y.; Fang, H. On the Characteristics Analysis and Tab Design of an 18650 Type Cylindrical $LiFePO_4$ Battery. *Appl. Therm. Eng.* **2021**, *182*, 116144. [CrossRef]
49. Santhanagopalan, S.; Guo, Q.; Ramadass, P.; White, R.E. Review of Models for Predicting the Cycling Performance of Lithium Ion Batteries. *J. Power Sources* **2006**, *156*, 620–628. [CrossRef]
50. Prada, E.; Di Domenico, D.; Creff, Y.; Bernard, J.; Sauvant-Moynot, V.; Huet, F. Simplified Electrochemical and Thermal Model of LiFePO4-Graphite Li-Ion Batteries for Fast Charge Applications. *J. Electrochem. Soc.* **2012**, *159*, A1508–A1519. [CrossRef]
51. Zhang, H.; Li, C.; Chen, H. Analysis of Prismatic Lithium-Ion Battery Degradation Based on an Electrochemical-Thermal-Degradation Model. *Int. J. Energy Res.* **2022**, *46*, 23658–23681. [CrossRef]
52. Prada, E.; Di Domenico, D.; Creff, Y.; Bernard, J.; Sauvant-Moynot, V.; Huet, F. A Simplified Electrochemical and Thermal Aging Model of LiFePO4-Graphite Li-Ion Batteries: Power and Capacity Fade Simulations. *J. Electrochem. Soc.* **2013**, *160*, A616–A628. [CrossRef]
53. Ploehn, H.J.; Ramadass, P.; White, R.E. Solvent Diffusion Model for Aging of Lithium-Ion Battery Cells. *J. Electrochem. Soc.* **2004**, *151*, A456. [CrossRef]
54. Jin, X.; Vora, A.; Hoshing, V.; Saha, T.; Shaver, G.; García, R.E.; Wasynczuk, O.; Varigonda, S. Physically-Based Reduced-Order Capacity Loss Model for Graphite Anodes in Li-Ion Battery Cells. *J. Power Sources* **2017**, *342*, 750–761. [CrossRef]
55. Choi, Y.S.; Kang, D.M. Prediction of Thermal Behaviors of an Air-Cooled Lithium-Ion Battery System for Hybrid Electric Vehicles. *J. Power Sources* **2014**, *270*, 273–280. [CrossRef]
56. Sahel, D.; Ameur, H.; Benzeguir, R.; Kamla, Y. Prediction of Heat Transfer Development in a Smooth Tube. *J. Eng. Phys. Thermophys.* **2018**, *91*, 682–687. [CrossRef]

57. Zhao, H.; Gao, B.; Ren, B.; Chen, H. Integrated Control of In-Wheel Motor Electric Vehicles Using a Triple-Step Nonlinear Method. *J. Frankl. Inst.* **2015**, *352*, 519–540. [CrossRef]
58. Wang, F.; Hao, N.; Song, L.; Chen, H. Triple-Step Nonlinear Control Design for Road Vehicles after a Tire Blow-out on the Highway. In Proceedings of the 2016 12th World Congress on Intelligent Control and Automation (WCICA), Guilin, China, 12–15 June 2016; pp. 1414–1419. [CrossRef]
59. Li, X.; Zhang, X.; Song, S. Effect of Delayed Impulses on Input-to-State Stability of Nonlinear Systems. *Automatica* **2017**, *76*, 378–382. [CrossRef]
60. Xu, M.; Wang, R.; Zhao, P.; Wang, X. Fast Charging Optimization for Lithium-Ion Batteries Based on Dynamic Programming Algorithm and Electrochemical-Thermal-Capacity Fade Coupled Model. *J. Power Sources* **2019**, *438*, 227015. [CrossRef]